Nanoscale Advances

ROYAL SOCIETY OF CHEMISTRY

REVIEW

View Article Online
View Journal | View Issue

Cite this: *Nanoscale Adv.*, 2025, **7**, 60

Porous carbon-nanostructured electrocatalysts for zinc–air batteries: from materials design to applications

Sanshuang Gao,†[a] Maolin Li,†[bc] Nianpeng Li,[b] Lei Zhang, *[c] Qian Liu,[d] Xinzhong Wang*[a] and Guangzhi Hu *[b]

Zinc–air batteries (ZABs) are pivotal in the evolution of sustainable energy storage solutions, distinguished by their high energy density and minimal environmental footprint. The oxygen electrode, which relies on sophisticated porous carbon materials, is critical to operational efficiency. This review scrutinizes oxygen reduction reaction (ORR) and oxygen evolution reaction (OER) processes in ZABs through advanced porous carbon applications. It delves into innovative synthesis techniques such as templating, chemical vapor deposition, and self-assembly that tailor pore structures for peak performance. The interactions between catalytic sites and carbon nanostructures, which significantly boost electrochemical performance, are highlighted. The manuscript discusses future strategies for overcoming current challenges by advancing catalytic efficiency and electrode design, emphasizing the integration of nano-engineering and materials science to foster ZABs with superior energy capacity and adaptability. Additionally, the review projects how ongoing research into carbon material properties could unlock new applications in other energy systems, potentially broadening the scope of ZAB technology. This paper integrates recent advancements in porous carbon materials, offering pivotal insights for next-generation high-performance ZAB development.

Received 13th October 2024
Accepted 4th November 2024

DOI: 10.1039/d4na00847b

rsc.li/nanoscale-advances

1. Introduction

The relentless increase in global energy demand,[1–3] coupled with significant environmental repercussions, underscores the urgent need for the continued development of advanced electrochemical energy storage and conversion systems. Various innovative renewable energy devices, including primary cells, secondary batteries, electrochemical fuel cells, and advanced supercapacitors, have been developed and successfully integrated into the global market.[4–9] Among the array of energy storage solutions, metal–air batteries emerge as a distinct category of electrochemical systems. These devices generate electrical energy through metal oxidation coupled with the concurrent reduction of atmospheric oxygen. Zinc–air batteries (ZABs) are particularly compelling due to the advantageous properties of zinc, such as its straightforward manufacturing process, abundant availability, excellent safety profile, and environmental compatibility.[10–12] ZABs boast a theoretical energy density exceeding 1086 W h kg^{-1}, five times higher than that of conventional lithium-ion batteries. This remarkable energy density has significantly increased the interest in ZABs within the scientific community (Fig. 1a and b).

However, the industrial realization of ZABs faces multifaceted intrinsic challenges, including suboptimal mass transport dynamics within oxygen electrodes and typically sluggish kinetic reactions of OER and ORR mechanisms. These constraints result in reduced cyclability of Zn–air cells, a significant challenge that resonates within scholarly discussions. To counter these prolonged kinetics, it is essential to incorporate oxygen electrodes with potent oxygen-evolving catalysts to accelerate both ORR and OER processes. This has become a focal point in contemporary research and technological advancement. Currently, the catalysts used for the ORR and OER predominantly include noble metals such as Pt, Ru, and Ir, known for their superior catalytic properties.[13,14]

Nevertheless, concurrent instability and elevated cost of noble metals substantially impede their broad application in ZAB air cathodes. Therefore, current research focuses on developing oxygen catalysts based on non-precious metals, aiming to combine operational efficiency with intrinsic catalytic durability. In contrast to the rotating disk electrode methodology, which is prevalently employed for evaluating the ORR in

[a]*Institute of Information Technology, Shenzhen Institute of Information Technology, Shenzhen 518172, China. E-mail: wangxz@sziit.edu.cn*

[b]*Institute for Ecological Research and Pollution Control of Plateau Lakes, School of Ecology and Environmental Science, Yunnan University, Kunming 650504, China. E-mail: guangzhihu@ynu.edu.cn*

[c]*School of Materials Science and Engineering, Anhui University of Science and Technology, Huainan 232001, China. E-mail: leizhang@aust.edu.cn*

[d]*Institute for Advanced Study, Chengdu University, Chengdu 610106, China*

† These authors contributed equally.

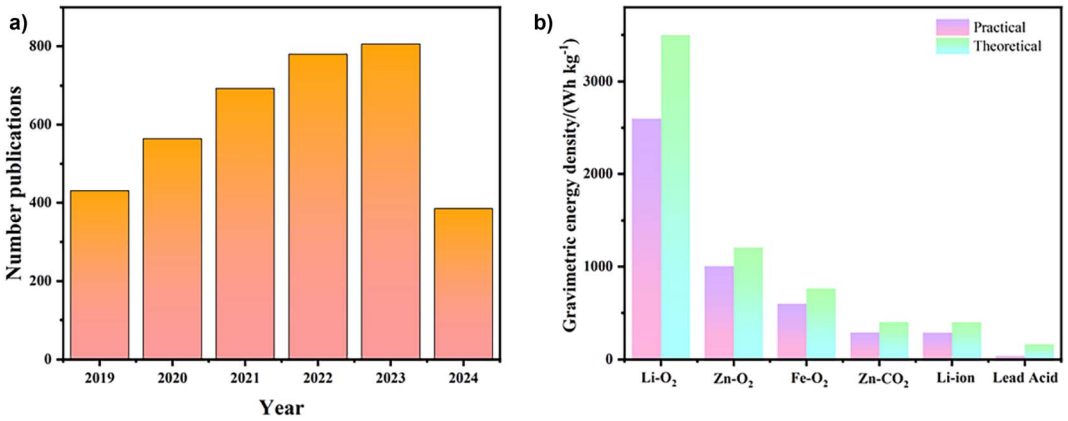

Fig. 1 Advances in ZAB research. (a) Publication trends on ZABs over the past five years. (b) Practical *versus* theoretical energy densities of different batteries.

academic research, the real-world deployment of ZABs is influenced by disturbances arising from material inconsistencies and air flux variations. Oxygen electrocatalysis take place across three phases: the solid phase (active catalytic materials), the liquid phase (electrolyte), and the gas phase (O_2). Enhancing oxygen diffusion and reinforcing the interfaces between these phases are vital for improving the overall performance of ZABs. In conclusion, integrating well-defined oxygen-catalytic sites with advanced nanoarchitectural designs is crucial. This approach expands the potential for developing advanced ZABs, highlighting a key area of contemporary research in electrochemical energy storage.

Recently, nanostructured porous carbon electrodes have gained attention as optimal oxygen electrodes for ZABs due to their large surface area, effective catalytic sites, hierarchical porous structure, durability, and cost-effectiveness. The porous configuration can substantially increase specific surface area, provide abundant active sites, and enhance the interaction surface between the catalyst and reactants. This architecture promotes uniform electrolyte penetration, improves gas diffusion, reduces concentration polarization, and prevents clogging, thereby aiding in the long-term stability of batteries. Moreover, hierarchical porous structures exhibit unique advantages in electrocatalysis by integrating the characteristics of micropores, mesopores, and macropores, thereby optimizing both the quantity and accessibility of active sites. Micropores provide abundant reaction centers and mesopores enhance their accessibility, while macropores facilitate overall mass transfer efficiency. This multi-scale structure can balance the abundance of active sites with mass transport requirements and potentially generate synergistic effects through interfacial phenomena, such as local electric field enhancement or the formation of novel active sites. These attributes and systematic design have led to numerous reviews in this field. The Shen group's work has provided deep insights into hierarchical architecture and reaction dynamics.[15] The Zhang group further explored the design of oxygen catalysts for ZABs, focusing on atomic-scale coordination and bifunctional carbon-based catalysts.[16] Huang *et al.* highlighted the development of flexible ZABs, emphasizing three-dimensional (3D) catalytic structures, solid-state electrolytes, and zinc anode design.[17] Although porous nanostructures of catalysts are crucial for improving OER and ORR performance, most traditional reviews remain deficient in understanding the relationship between the structure and function. These gaps cover catalytic site design, nanoscale structures, and fabrication methods, causing porous catalysts to remain underexplored in comprehensive reviews. Therefore, this review provides a focused discussion on the systematic analyses of the latest innovations in flexible and high-power ZABs, aiming to assist readers in understanding the advantages, challenges, and prospective directions of porous catalysts.

This study delves into the nanoarchitectural advancements of porous carbon electrodes within zinc–air battery (ZAB) systems, emphasizing their role in facilitating enhanced oxygen catalysis. We detail the operational dynamics and foundational principles of porous carbon in oxygen electrodes, applied in primary and secondary ZAB configurations. We employ diverse methods to engineer these electrodes, focusing on metal-free heteroatom integration, single-atom metal sites, and metal alloys and complexes in the porous carbon matrix. The evolution of carbon substrates is directed towards optimizing the functionality of oxygen electrodes. The discussion extends to various synthetic approaches, detailed analytical characterization, and the complex interplay between the porous carbon's catalytic sites, its nanoscale structure, and overall electrochemical performance. Additionally, the manuscript highlights recent innovations in designing flexible, high-capacity ZABs with porous carbon, tailored for real-world applications. The paper provides a comprehensive review of the future directions, challenges, and strategic insights into the deliberate design of nanostructured porous carbon electrodes for zinc–air energy systems. This scholarly effort aims to foster significant advancements in the kinetics and efficiency of ZABs, leveraging porous catalysts with unique properties.

2. Mechanisms and principles of air electrodes in ZABs

2.1. Working mechanism of ZABs

Within a rechargeable ZAB, anodic zinc and cathodic air electrode are juxtaposed, separated by a selectively permeable membrane immersed in an alkaline electrolyte. The electrochemical functionality of the battery is characterized by two principal catalytic reactions at the interface of the air electrode: the ORR during the discharge cycle and the OER during the charging cycle.[18,19] At the onset of discharge, oxidation of the zinc anode occurs, interacting with hydroxyl ions (OH^-) to generate soluble zincate ions ($Zn(OH)_4^{2-}$), as specified in eqn (1). This reaction leads to a substantial concentration gradient of zincate ions, culminating in their conversion to insoluble zinc oxide, as indicated in eqn (2). As depicted in Fig. 2a, oxygen molecules navigate through the porous structure of the cathode, engaging at the triphase boundary where the solid electrode, liquid electrolyte, and gas phase meet, as represented in eqn (3). These interactions facilitate the movement of hydroxyl ions through the electrolyte from the air cathode to the zinc anode, propelling the associated redox reactions (eqn (3)). The theoretical upper limit of the ZAB's voltage, approximately 1.65 volts, is established by the electrochemical interactions at both electrodes within this alkaline context, as outlined in eqn (4). During the recharging process, illustrated in Fig. 2b, reverse reactions reduce zincate ions back to metallic zinc while concurrently releasing oxygen, as described in eqn (6)–(9).[20]

Discharge

$$\text{Anode: } Zn + 4OH^- \rightarrow Zn(OH)_4^{2-} + 2e^- \quad (E^0 = -1.25\ \text{V } \textit{vs.}\ \text{SHE}) \tag{1}$$

$$Zn(OH)_4^{2-} \rightarrow ZnO + H_2O + 2OH^- \tag{2}$$

$$\text{Cathode: } O_2 + 2H_2O + 4e^- \rightarrow 4OH^- \quad (E^0 = +0.4\ \text{V } \textit{vs.}\ \text{SHE}) \tag{3}$$

$$\text{Overall reaction: } 2Zn + O_2 \rightarrow 2ZnO \quad (E_{cell} = E^0_{cathode} - E^0_{anode} = +1.65\ \text{V}) \tag{4}$$

$$\text{Parasitic reaction: } Zn + 2H_2O \rightarrow Zn(OH)_2 + H_2 \tag{5}$$

Charge

$$\text{Anode: } ZnO + H_2O + 2OH^- \rightarrow Zn(OH)_4^{2-} \tag{6}$$

$$Zn(OH)_4^{2-} + 2e^- \rightarrow Zn + 4OH^- \tag{7}$$

$$\text{Cathode: } 4OH^- \rightarrow O_2 + 2H_2O + 4e^- \tag{8}$$

$$\text{Overall reaction: } 2ZnO \rightarrow 2Zn + O_2 \tag{9}$$

2.2. Basics of ORR and OER mechanisms

In aqueous alkaline environments, the ORR is differentiated into two unique electrochemical pathways: a two-electron mechanism (eqn (10)) that transiently generates superoxide intermediates and a four-electron mechanism (eqn (11)) that results in OH^- production. The latter is generally favored for its superior energy and power efficiencies, contrasting sharply with the former, which forms corrosive peroxide intermediates and yields less energy efficiency. In such media, the OER process entails the formation of metal oxyhydroxide (M-OOH) intermediates, decomposing to release molecular O_2 and water. The OER is a multifaceted process involving various intermediates such as metal hydroxides (M-OH) and M-OOH, critical in shaping the overall electrocatalytic performance.[21] Insights into the interplay between kinetic behavior and thermodynamic stability, particularly concerning the redox dynamics of the metal centers, can be gleaned from a volcano plot. This analytical approach highlights the intricate relationships within the electrochemical reactions involving oxygen in the ORR and OER. The dual-functionality of the ORR/OER presents a significant challenge for catalysis. The chosen substrate must

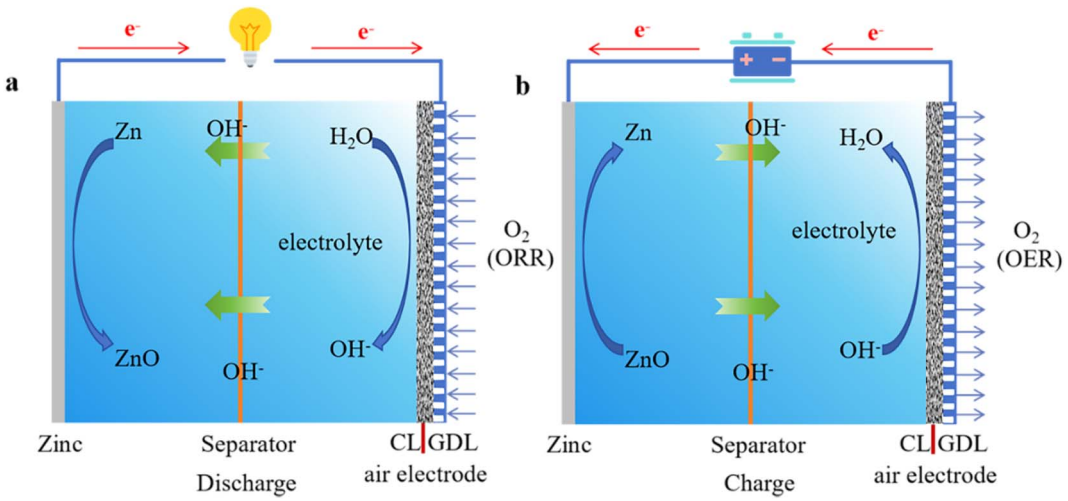

Fig. 2 (a) Schematic illustration of a ZAB operating in the discharge mode. (b) Schematic representation of a ZAB in the charging mode.

withstand a highly corrosive environment and efficiently facilitate O–O bond cleavage while promoting the release of oxygen from the catalyst surface. The activation of O_2 primarily involves the transfer of protons and electrons to form OOH, which then splits into O and OH at the catalytic interface. To achieve bifunctional activities, anchoring the oxyhydrogen radical (OOH) firmly on the catalyst surface is crucial to ensure minimal adherence of oxygen and hydroxyl species, which can facilitate rapid desorption of water and oxygen and enhance catalytic efficiency.

$$O_2 + H_2O + 2e^- \rightarrow HO_2^- + OH^- \quad (10)$$

$$O_2 + 2H_2O + 4e^- \rightarrow 4OH^- \quad (11)$$

Although advancements in ZABs have generated significant enthusiasm, their commercial applications are limited by several challenges. A major issue is the short lifespan of ZABs, primarily due to the deactivation of the air catalyst during operation, leading to reduced current density and increased overpotential. These increases in potential accelerate oxidation and corrosion of the oxygen electrocatalysts. The inherent fragility of the porous framework within the air electrode exacerbates these issues, resulting in decreased structural robustness to withstand the gas evolution phenomena of the OER during the charging cycle.[22] This leads to mechanical erosion and reduced vitality of the electrode components, ultimately deteriorating battery performance. The performance of ZABs can also be significantly hindered by the formation of dendrite-branch-like metal structures that cause short circuits and the release of hydrogen gas due to unwanted side reactions (eqn (5)). These side reactions reduce efficiency and pose safety concerns by depleting the aqueous content in the electrolyte, leading to the precipitation of corrosive products on the Zn electrode, thus shortening the battery's operational life. A high electrolyte concentration introduces technical challenges, including reduced ionic conductance and increased Zn solubility, which limit the reactivity of the Zn anode and promote electrolyte vaporization, thereby restricting the development of rechargeable ZABs. Additionally, the interaction of atmospheric CO_2 with electrolytes results in the formation of carbonate deposits that impede ionic transport and air permeation at the air electrode interface. Extensive research has been dedicated to exploring catalytic materials, optimizing electrode configurations, studying electrolyte complexities, and understanding Zn anode properties to enhance cycling efficiency and increase the energy yield of rechargeable ZABs.

3. Pore structure

3.1. Structure of porous materials

In the realm of ZAB research, the pore size of porous carbon materials is crucial to their functional performance. These materials are classified into three distinct categories based on pore size: microporous (less than 2 nm), mesoporous (2 to 50 nm), and macroporous (greater than 50 nm). Each category not only dictates the physical structure of the materials but also significantly impacts their chemical activity and operational effectiveness in ZABs. The small pore size of microporous materials makes them particularly suitable for confining active sites of single-atom catalysts,[23–27] which is crucial for the ORR and OER. These two reactions are the core electrochemical processes of ZABs, directly affecting the energy output and charge–discharge efficiency. Although diffusion limitations within micropores might slow reaction rates, they can also enhance catalytic efficiency by increasing the residence time of reactants at active sites. Mesoporous materials can optimize diffusion speed and mass transfer and improve reaction kinetics for the battery.[28–34] These materials are ideal for handling large molecules or complex electrochemical reactions, as their pore size is sufficient to accommodate larger molecular structures, preventing pore blockage. Macroporous materials are well-suited for applications requiring rapid mass transfer and high fluidity, particularly under high-load conditions in ZABs.[35–39] The open structure of these materials promotes fast gas exchange and electrolyte flow, thereby enhancing overall battery performance. Table 1 presents comparison of ZAB performances with varying pore sizes.

Table 1 Comparison of ZABs performance with different pore sizes

Catalyst material	Porous structure (nm)	ORR/ ($E_{1/2}$, V)	OER/ ($E_{j=10}$, V)	Peak power density (mW cm^{-2})	Specific capacity (mA h g_{Zn}^{-1})	References
PDA–Fe-900	5	0.84	1.67	163.0	802.1	40
La–Fe/NC		0.879		179.8	755	41
Co–CoN_4@NCNs	1.5, 2–6	0.83	1.54	118.8	776.7	42
P-$MnCo_2O_4$@PWC	1.3–4.0	0.87	1.53	160	811.3	43
Co_H SA/NC	~1.5	0.874	1.63	191.7	745	44
ZnCoFe-TAC/SNC	4	0.901	1.603	304	760	45
Dy_2O_3–Fe/NC	20–80	0.914	1.626	225		46
Co@C–O–Cs	2	0.82	1.524	106.4	720.7	47
Co_4N@CoON/PCGN	1, 2–5	0.855	1.595	153		48
J-CeO_2/ZCS		0.87	1.52	168.7	785.9	49
CoS/Fe_3S_4@SNCP	1.14, 2.27	0.85	1.5	272	831	50
Fe_5Co_5@NPC	4.5	0.904	1.48	117.6	808	51
β-FeCo-PCNF	<2	0.90	1.495	196.5	756	52
CoP_3/CeO_2/C-2	3–4	0.752	1.569	150	767.7	53

3.1.1. Microporous structure. The microporous configuration substantially increases the material's specific surface area, providing numerous active sites and enhancing the interaction surface between the catalyst and reactants. This significantly boosts the electrocatalytic performance for both the ORR and the OER. Zhang *et al.*[54] synthesized CoFe alloy nanoparticles *via* a one-step method followed by carbonization, imbuing the material with densely microporous N,O co-doped multilayer graphitic shells that improve the catalytic effectiveness of the CoFe@NOC catalyst in both reactions. This catalyst demonstrated a reduced overpotential (ΔE) of 0.678 V. Utilizing this catalyst, the ZAB displayed substantial stability, achieving a power density exceeding 200 mW cm^{-2} and a specific capacity of 829.5 mA h g^{-1} and maintaining excellent cycling stability over prolonged periods. Tan *et al.*[55] encapsulated sub-nanometer CoO_x clusters (0.86 nm) within the micropores of N-doped carbon derived from ZIF-8. This effectively prevented agglomeration and performance decline due to the material's high specific surface energy. The microporous framework facilitated the integration of CoO_x nanoclusters with Co–N_x, enhancing the electronic structure. The optimized 0.05 CoO_x@PNC catalyst exhibits superior bifunctional catalytic performance in ZABs, achieving 0.98 V ORR onset potential, 0.88 V $E_{1/2}$, and 1.55 V OER overpotential at 10 mA cm^{-2}. Moreover, this catalyst displayed exceptional electrochemical characteristics, achieving a peak power density of 157.1 mW cm^{-2}, a specific capacity of 887 mA h g_{Zn}^{-1}, and cycling stability exceeding 200 hours. Shen *et al.*[25] fabricated an FeSA/N-PSCS catalyst through a nitrogen-enriched heterocyclic-regulated supramolecular coordination self-assembly strategy (Fig. 3a), and the single Fe atoms were stabilized on N-rich porous submicron carbon spheres. The Fe/Zn–Ad complex was subjected to high-temperature pyrolysis, creating a highly porous structure with substantial internal pore volume and a specific surface area reaching 1062 m^2 g^{-1} (Fig. 3c). The abundant microporous structure significantly increased the exposure of active sites within the catalyst, allowing the Fe–N_4 active centers to participate more effectively in the ORR. Density functional theory (DFT) calculations indicated that the microporous structure optimized the adsorption of oxygen intermediates on the Fe–N_4 active sites, reducing the reaction overpotential. The observed enhancement in catalytic activity is principally

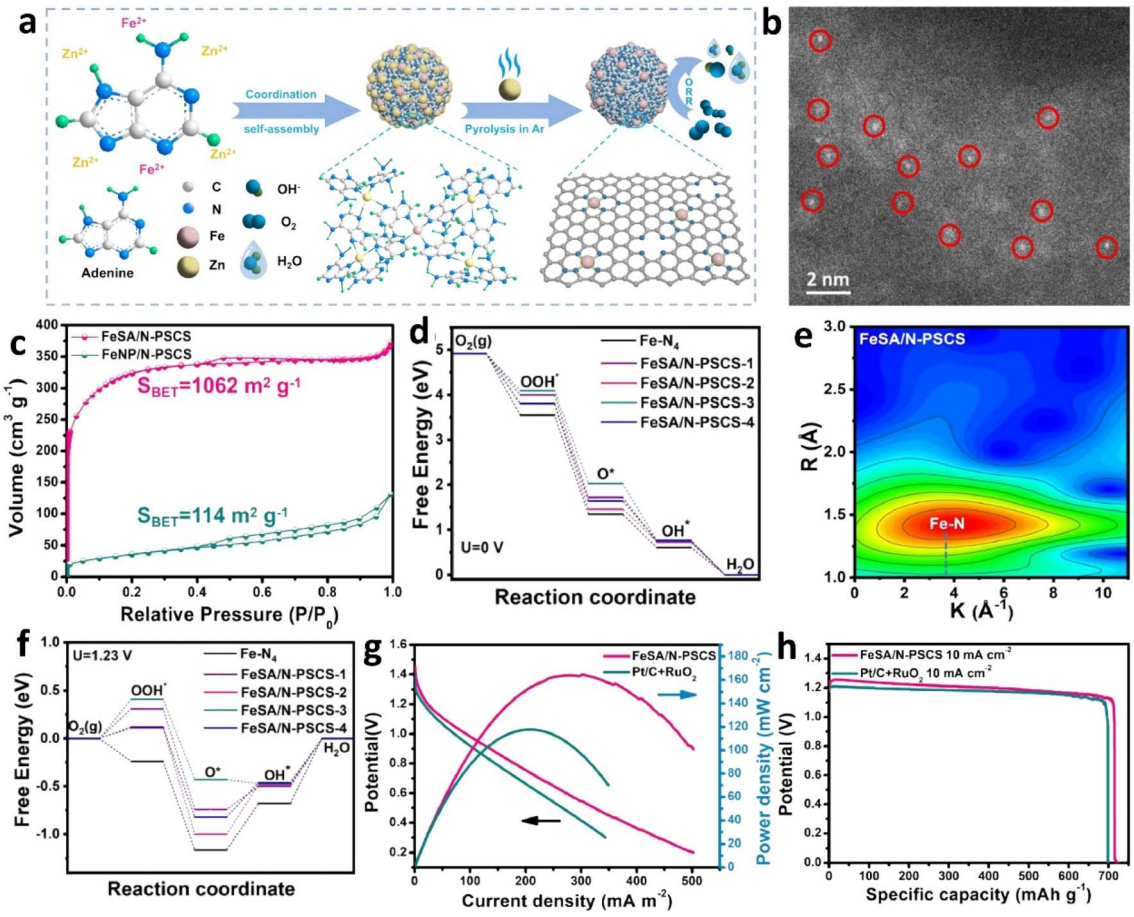

Fig. 3 (a) Synthesis of an FeSA/N-PSCS catalyst. (b) AC-HAADF-STEM image. (c) N_2 adsorption–desorption isotherms. (d) Gibbs free energy at $U = 0$ V for Fe–N_4 and FeSA/N-PSCS-*X*. (e) Wavelet transforms of EXAFS signals. (f) Gibbs free energy at $U = 1.23$ V for Fe–N_4 and FeSA/N-PSCS-*X*. (g) Polarization and power density curves of ZABs with FeSA/N-PSCS and Pt/C + RuO_2 catalysts. (h) Discharge-specific capacity of ZABs at 10 mA cm^{-2}. Reproduced with permission from ref. 25 Copyright 2024, Elsevier.

ascribed to the nitrogen-doped carbon residing within the micropores. This modification optimizes the electronic milieu around the Fe–N_4 active sites and enhances the stabilization of oxygen intermediates' adsorption, as depicted in Fig. 3d–f. Employing the FeSA/N-PSCS catalyst, the battery achieved 164.5 mW cm^{-2} peak power density and 725.3 mA h g^{-1} specific capacity, as illustrated in Fig. 3g and h. Moreover, it exhibited enduring stability over prolonged cycling tests. Advanced characterization techniques such as aberration-corrected high-angle annular dark-field scanning transmission electron microscopy (AC-HAADF-STEM) and extended X-ray absorption fine structure (EXAFS) further confirmed the high dispersion of Fe single atoms and the superiority of the microporous structure (Fig. 3b–e).

3.1.2. Mesoporous structure. While microporous materials are exceptional at increasing surface area, mesoporous materials provide superior reactant accessibility and reduced mass transfer resistance. Xie *et al.*[56] utilized NH_2-MIL-101(Al) as a precursor to prepare a mesoporous Fe single-atom catalyst (Fe SAC-MIL101-*T*) through a two-step pyrolysis and acid etching process (Fig. 4a and b). Initially, NH_2-MIL-101(Al) was pyrolyzed under a nitrogen atmosphere at temperatures ranging from 800 to 1100 °C to obtain a N-doped carbon material (NC-MIL101-*T*). Subsequent treatment with dilute hydrochloric acid removed amorphous aluminum, creating a rich mesoporous structure. The Fe(II)–phenanthroline complex was consistently adsorbed onto internal and external surfaces of NC-MIL101-*T*, subsequently undergoing a second pyrolysis process at 800 °C to establish well-dispersed FeN_x single-atom sites. Subsequent BET analysis demonstrated that Fe SAC-MIL101-1000 possessed a specific surface area of 1017 m^2 g^{-1} and an external surface area of 376 m^2 g^{-1}, characterized by type IV isotherm properties, indicative of a predominantly mesoporous structure, as illustrated in Fig. 4c and d. Within a 0.1 M KOH solution, the $E_{1/2}$ achieved was 0.94 V, shown in Fig. 4e. Employing this catalyst, the ZABs achieved a peak power density of 192.3 mW cm^{-2} and an energy density of 984.2 W h kg_{Zn}^{-1}, as depicted in Fig. 3f and g. Wang *et al.*[57] crafted a mesoporous Fe–Zn/N/C/MWCNTs-800 electrocatalyst through a dual-stage process involving pyrolysis and acid etching, utilizing ferric nitrate and tannic acid as precursors. This catalyst achieved an $E_{1/2}$ of 0.858 V in 0.1 M KOH. Moreover, the ZAB employing the Fe–Zn/N/C/MWCNTs-800 catalyst delivered an outstanding performance, characterized by 1.46 V open-circuit voltage and 259 mW cm^{-2} peak power density and maintained cycling stability for 180 hours. The synthesis was further enhanced by ZIF-67 and

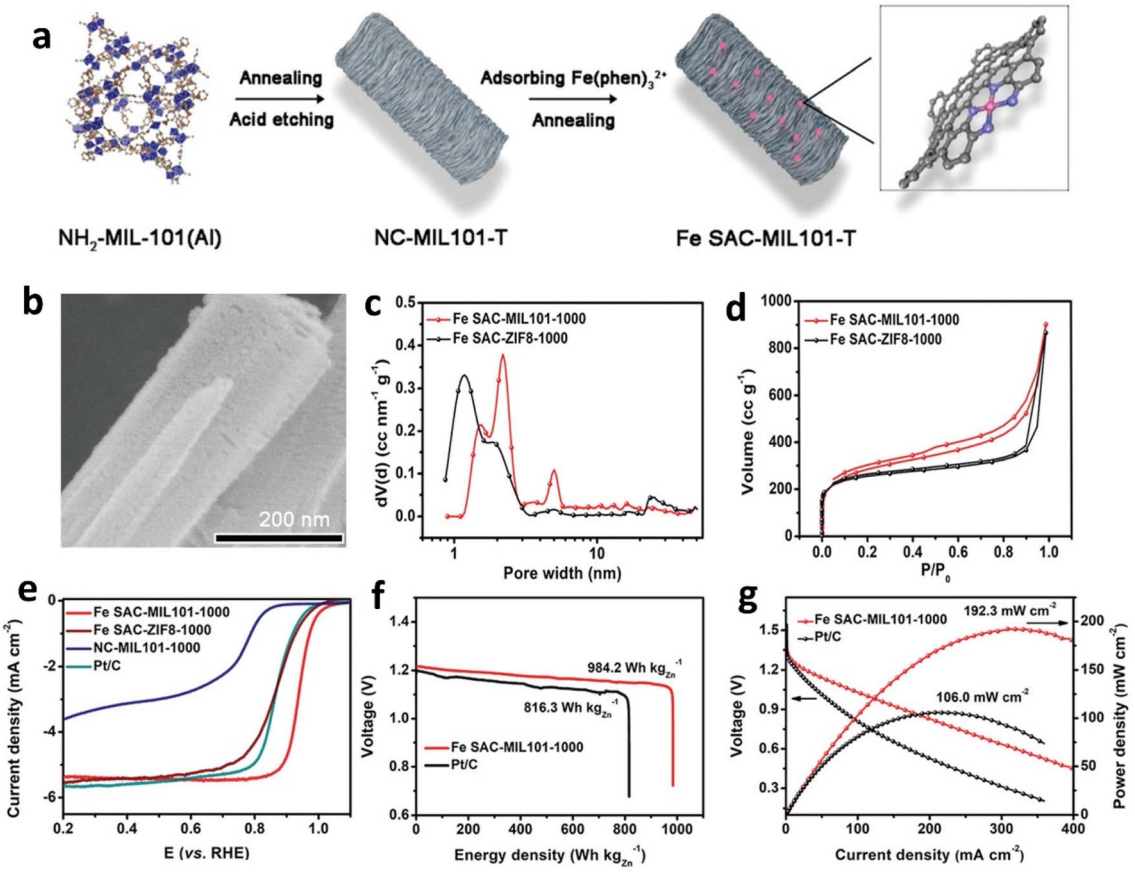

Fig. 4 (a) Formation of Fe SAC-MIL101-*T*. (b) Scanning electron microscope (SEM) images of NC-MIL101-1000. Pore size distribution (c) and N_2 adsorption/desorption isotherms (d) of Fe SAC-MIL101-1000 and Fe SAC-ZIF8-1000. (e) Comparison of LSV performance of Fe SAC-MIL101-1000 with that of other samples. Discharge/power density curves (f) and discharge profiles (g) at 20 mA cm^{-2} for aqueous ZABs using Fe SAC-MIL101-1000 and Pt/C air electrodes. Reproduced with permission from ref. 56 Copyright 2021 Wiley-VCH.

incorporating the surfactant P123. Liang *et al.*[58] successfully synthesized onion-like carbon nanosphere encapsulated Co, N-doped carbon (OLC/Co–N–C) materials. The introduction of P123 led to the formation of mesoporous and microporous structures, significantly increasing the specific surface area of the material to 388 $m^2 g^{-1}$, compared to 246 $m^2 g^{-1}$ for Co–N–C without the surfactant. OLC/Co–N–C exhibited an $E_{1/2}$ of 0.855 V. For the OER, OLC/Co–N–C showed an overpotential of 344 mV. Theoretical analyses have demonstrated that the integration of a mesoporous structure with highly curved carbon nanospheres substantially augments the electrocatalytic efficacy of the active sites within the material.

3.1.3. Macroporous structure. Macroporous carbon materials significantly enhance mass transport efficiency, demonstrating exceptional performance at high current densities. This architecture promotes uniform electrolyte penetration, improves gas diffusion, reduces concentration polarization, and prevents clogging, thereby aiding in the long-term stability of batteries. Although they possess a relatively lower specific surface area, macroporous structures offer greater potential for designing complex catalytic systems and supporting large-sized nanoparticles.[59,60] Li *et al.* engineered a single-atom B–N_3 structure supported by ordered macroporous carbon, utilizing hydrogen-bonded organic frameworks as precursors for carbon and nitrogen and SiO_2 spheres as scaffolds.[61] The catalyst displayed 0.94 V onset potential and 0.81 V $E_{1/2}$. DFT calculations demonstrated that the B–N_3 structure markedly enhances catalytic performance by furnishing abundant OOH^- and OH^- adsorption sites at the boron center, thus facilitating intermediate formation. Yang *et al.* developed a method for synthesizing vertically aligned CoFe alloy-embedded nitrogen-doped carbon nanosheet arrays on NF *via in situ* self-templating ion adsorption and pyrolysis.[29] This macroporous structure allows the catalyst to maintain a low overpotential even at high current densities, significantly enhancing the overall performance and durability of ZABs. The CoFe–NiFe/NC catalyst exhibited a specific energy of up to 990.3 W h kg_{Zn}^{-1} at 10 mA cm^{-2} and showed no significant decay over 400 hours of cycling. Zeng *et al.*[62] engineered a nitrogen and phosphorus co-doped carbon macroporous fiber embedded with atomically dispersed Cu and Zn atoms. This material's 3D macroporous structure facilitates uniform electric field distribution and reduces local current density, providing ample space for zinc deposition and volume changes.

Hong *et al.* advanced the synthesis of nanomaterials (Fig. 5a) by initiating their process with a binary mixture of cobalt acetate and trisodium citrate.[38] This precursor mixture was subsequently integrated with potassium ferrocyanide to synthesize a cobalt–iron Prussian Blue Analog (PBA) nanoframe. The nanoframe was then encapsulated in polytriazine, followed by incorporation of a molybdenum precursor. The composite material underwent thermal decomposition under a nitrogen atmosphere, yielding an N-doped Fe–Co/Mo_2C carbon nanoframe. This innovative approach promoted the formation of a macroporous structure (Fig. 5b and c) through the strategic disintegration and reorganization of the polytriazine and carbon matrix. This macroporous carbon matrix is instrumental in shielding active sites from electrolyte-induced corrosion and preventing the agglomeration or deactivation of catalysts during prolonged operational periods. In performance metrics, the Fe–Co/Mo_2C@NCF-based ZAB exhibited a specific capacity of 694.0 mA h g_{Zn}^{-1} (Fig. 5d). Following 240 hours of charge–discharge cycling at 5 mA cm^{-2}, the ZAB featuring the Fe–Co/Mo_2C@NCF cathode displayed a modest increase in the voltage gap to 0.92 V, thereby underscoring the catalyst's substantial efficacy in facilitating both the OER and ORR.

3.1.4. Hierarchical porous structures. Hierarchical porous structures exhibit unique advantages in electrocatalysis by integrating the characteristics of micropores, mesopores, and macropores, thereby optimizing both the quantity and accessibility of active sites. Micropores provide abundant reaction centers and mesopores enhance their accessibility, while macropores facilitate overall mass transfer efficiency. This multi-scale structure balances the abundance of active sites with mass transport requirements but also potentially generates synergistic effects through interfacial phenomena, such as local electric field enhancement or the formation of novel active sites.[63] Liu *et al.* developed a novel hierarchical porous structure by *in situ* growth of carbon nanotubes on worm-like layered porous carbon, onto which Fe/Fe_3C nanoparticles were deposited.[64] This unique multi-tiered pore system significantly enhanced the performance of ZABs. Benefiting from this optimized hierarchical porous architecture, the resulting Fe-2-WNPC-NCNTs demonstrated exceptional electrochemical properties. Utilized as the cathode catalyst in ZABs, this material exhibits a peak power density of 101.3 mW cm^{-2} and an energy density of 719.1 W h kg^{-1} when subjected to a high discharge of 50 mA cm^{-2}.

Gong *et al.* utilized ZIF-67 as a precursor and crafted a hierarchical pore system featuring macropores, mesopores, and micropores through a meticulously designed synthesis strategy.[13] TEM observations further confirmed the presence of this multi-tiered pore structure. TEM images of HP-Au@ZIF-67 vividly revealed the internal macroporous structure, while pore size distribution charts distinctly displayed the three different scales of pores: micropores originating from the ZIF-67 framework, mesopores formed by the stacking of Co_xS_y nanosheets, and macropores generated using polystyrene sphere templates. This tiered pore architecture played a synergistic role in the electrocatalytic process, where HP-Au@Co_xS_y@ZIF-67 demonstrated exceptional performance in the OER. This material required only 340 mV overpotential and exhibited a low Tafel slope of 42 mV dec^{-1}. Importantly, the catalyst displayed outstanding long-term stability, maintaining 95% of its initial current density after continuous operation for 25 000 seconds. Guo *et al.* adjusted the mass ratio of ferrocene and melamine, achieving precise control over the morphologies of materials ranging from nanotubes and nanosheets to microspheres.[65] They synthesized a hierarchical porous Fe_2O_3/Fe_5C_2/Fe–N–C-3 composite electrocatalyst, which exhibited an $E_{1/2}$ of 0.87 V and a maximum current density of 5.34 mA cm^{-2}. When used as the cathode catalyst in a ZAB, this battery demonstrated an OCV of 1.55 V and a peak power density of 151.3 mW cm^{-2}. Utilizing dye sludge as a precursor, Peng *et al.* engineered a novel ZnS-

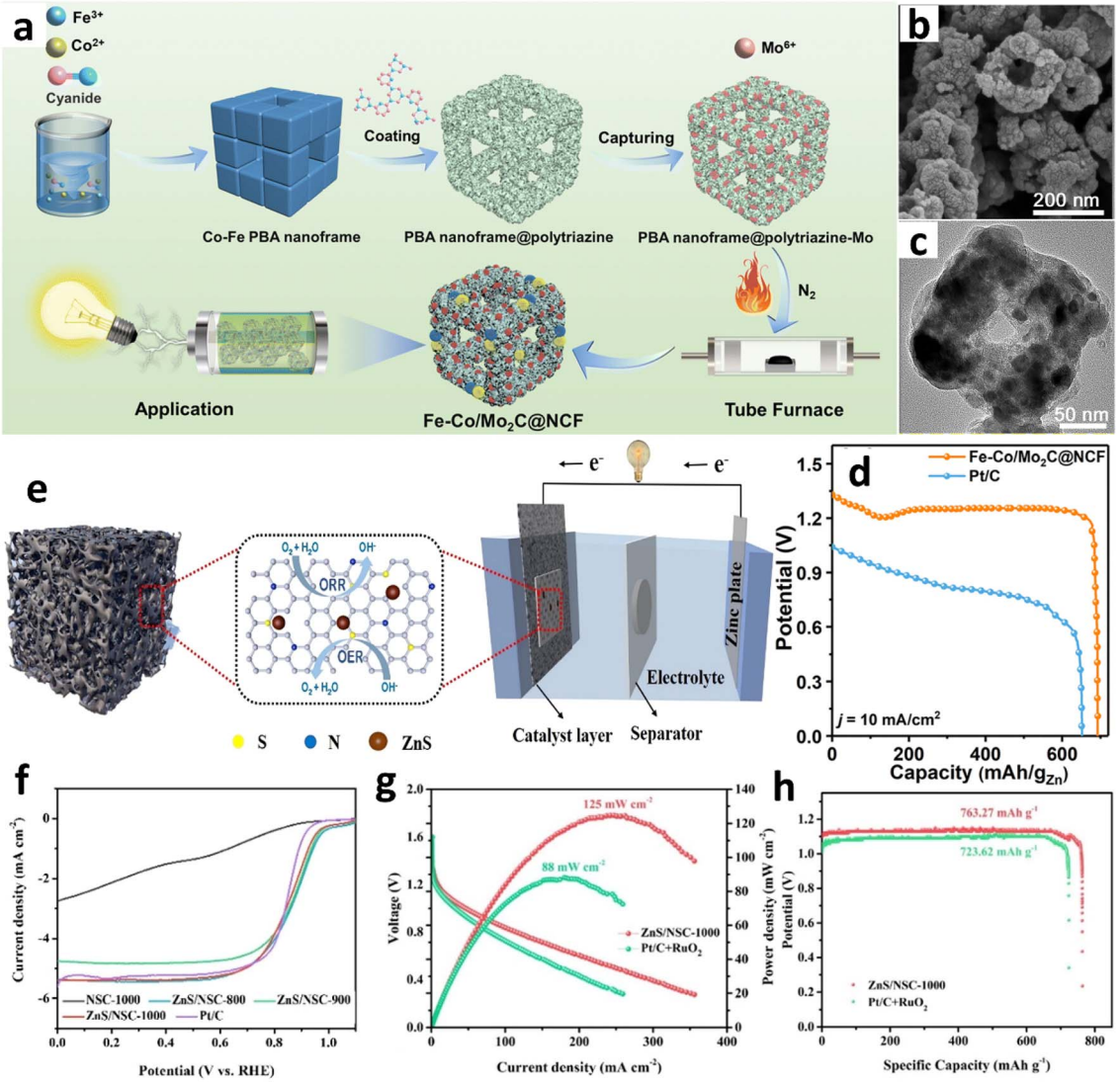

Fig. 5 (a) Synthesis of an Fe–Co/Mo_2C@NCF catalyst. (b) SEM images and (c) transmission electron microscope (TEM) images of Fe–Co/Mo_2C@NCF. (d) Galvanostatic discharge profiles *versus* specific capacity. Reproduced with permission from ref. 38 Copyright 2023, Royal Society of Chemistry. (e) ZnS/NSC-1000 catalyst for ZABs. (f) LSV curves of ZnS/NSC-1000 and comparison samples. (g) Specific capacity and energy density (h) of ZnS/NSC-1000 and Pt/C + RuO_2-based batteries at 10 mA cm^{-2}. Reproduced with permission from ref. 30 Copyright 2022, Elsevier.

enhanced, N and S co-doped porous carbon material (ZnS/NSC) through a pyrolysis process facilitated by $ZnCl_2$ (Fig. 5e).[30] This hierarchical porous structure demonstrates advantages in three aspects: firstly, macropores provide rapid mass transport channels; secondly, mesopores increase the ion-accessible surface area; and lastly, micropores further expose additional catalytically active sites. Remarkably, within the ZnS/NSC-1000 sample, which was subjected to a pyrolysis process at 1000 °C, ZnS nanoparticles are evenly embedded throughout the N and S co-doped porous carbon matrix. Benefiting from this optimized hierarchical porous structure, ZnS/NSC-1000 achieves an $E_{1/2}$ of 0.86 V and an OER potential of merely 1.62 V (Fig. 5f). Furthermore, a ZAB employing ZnS/NSC-1000 exhibits exceptional performance: a power density of 125 mW cm^{-2}, a specific capacity of 763.27 mA h cm^{-2} (Fig. 5g and h), and cycling stability exceeding 85 hours at 10 mA cm^{-2}.

In ZAB research, the architecture of porous carbon materials critically influences battery performance. This section comprehensively examines how various pore dimensions – microporous, mesoporous, and macroporous – affect electrochemical activity and mass transfer efficiency, highlighting the profound impact of the material's pore structure on battery efficacy. Future investigations should prioritize the development of innovative synthesis techniques designed to streamline manufacturing processes, reduce costs, and improve the long-term stability of materials. Moreover, by exploring the interplay between porous structures and electrochemical activity, there is potential to further refine material performance, tailoring it to meet specific application demands.

3.2. Methods for synthesizing porous carbon structures

Creating porous structures in carbon materials is vital for ZAB efficiency enhancement. Key synthesis methods encompass templating, sol–gel processes, and activation techniques.[66–85] Each approach has distinct characteristics, allowing for precise control over pore dimensions, increasing specific surface area, or forming specialized structures. Advanced technologies such as chemical vapor deposition (CVD) and chemical etching methods have introduced new possibilities for accurately manipulating porous structures.[86,87] Choosing the right method necessitates careful evaluation of specific application requirements and desired characteristics. As technology progresses, more precise control of porous structures is expected to improve ZAB performance.

3.2.1. Template method. Template methods, involving the integration of template materials during preparation to create porous structures, have emerged as a vital technique in synthesizing porous carbon materials. This method's core principle is to utilize the distinctive morphology and structural features. By duplicating and eliminating the template, these methods allow precise control over the pore size, distribution, and channel morphology.

When utilizing MOF precursors as templates, their highly ordered pore architectures are partially retained during the pyrolysis process and subsequently transformed into the porous structures of the resultant carbon materials.[88] Xiao and colleagues engineered hierarchical sub-microporous carbon materials utilizing ZIF-67, ZIF-8, and Zn/Co-ZIF frameworks.[70] After impregnation with chloroplatinic acid and high-temperature secondary annealing, they synthesized efficient catalysts such as PtCo/CoNC, PtZn/ZnNC, and Pt_3Co/CoNC. In evaluations with zinc–air batteries, Pt_3Co/CoNC, employed as an air electrode, demonstrated a peak power density of 187 mW cm^{-2} and a specific capacity of 768.9 mA h g^{-1} at 5 mA cm^{-2}. Qi *et al.* devised a stratified nitrogen doping approach, employing CoZn-ZIFs as both precursors and structural templates for the fabrication of cobalt nanoparticle catalysts enveloped within nitrogen-deficient graphene and nitrogen-enriched carbon nanotubes (Co@CNTs@NG).[89] This catalyst demonstrated an $E_{1/2}$ of 0.86 V and attained a peak current density of 5.5 mA cm^{-2}.

The most widely recognized hard template approach employs inorganic materials, such as silica (SiO_2), magnesium oxide (MgO), and polystyrene (PS), as templates. This method

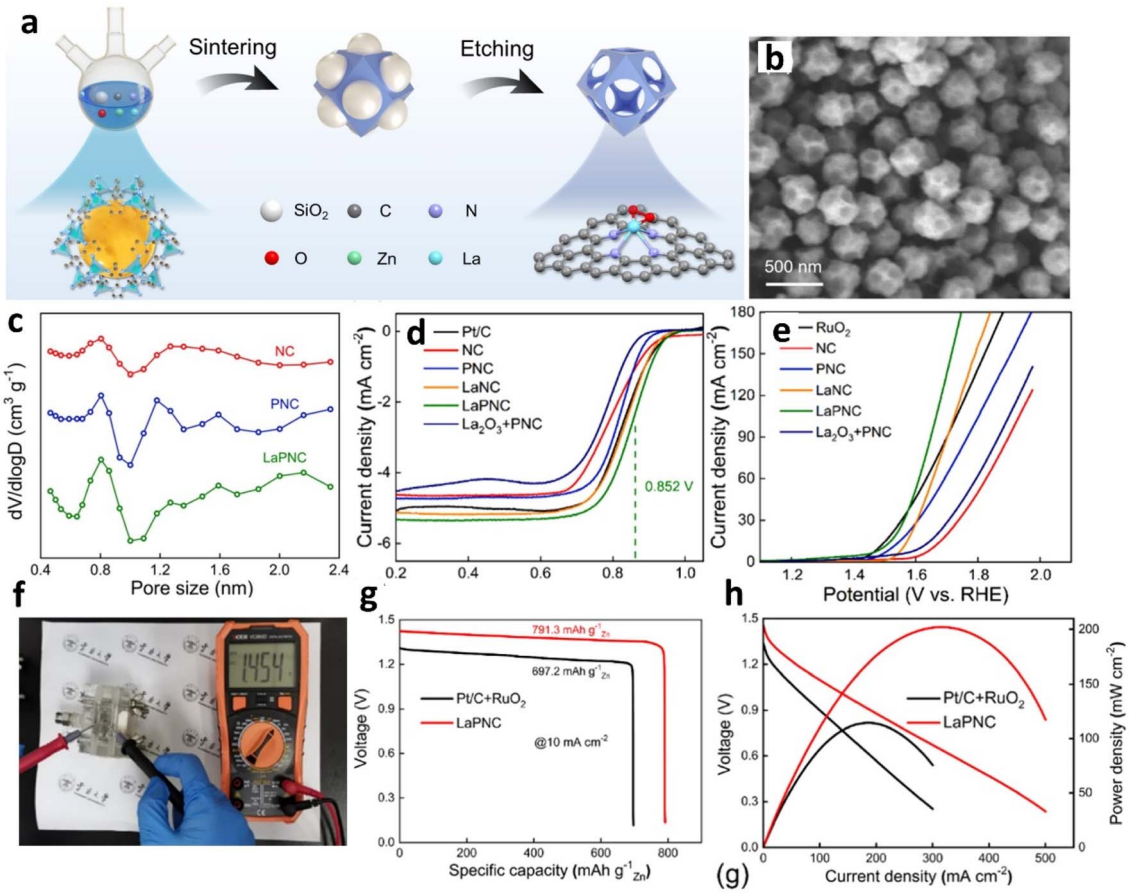

Fig. 6 (a) Formation process of LaPNC. (b) SEM image of LaPNC. (c) Micropore size analysis of LaPNC and its comparison samples. (d) LSV curves for various materials as ORR catalysts at 1600 rpm and (e) as OER catalysts. (f) Open-circuit voltage of LaPNC. (g) Discharge polarization and power density curves, and (h) specific capacities at 10 mA cm^{-2} for ZABs with LaPNC and Pt/C + RuO_2 air cathodes. Reproduced with permission from ref. 90 Copyright 2022, Elsevier.

allows for precise control over pore size and distribution, ensures high reproducibility and consistency, and contributes to the material's mechanical strength and stability. Hu *et al.* developed an innovative synthesis approach, combining the SiO_2 hard-templating (Fig. 6a) methodology with a metal node exchange strategy, to fabricate a lanthanum-doped nitrogen-rich carbon catalyst (LaPNC) exhibiting a unique hierarchical micro–meso–macroporous architecture.[90] Morphological characterization *via* SEM and TEM (Fig. 6b) revealed a rhombic dodecahedral structure featuring uniformly distributed macropores on each facet. Quantitative pore analysis corroborated these observations, with the plot method indicating predominant micropore dimensions of 0.8 and 1.2 nm, while Barrett–Joyner–Halenda (BJH) analysis elucidated primary mesopore diameters of 9.3 and 15.9 nm (Fig. 6c). The advantageous multi-scale porosity of LaPNC manifested in exceptional electrocatalytic performance.

In the realm of the ORR, the catalyst exhibited an exemplary $E_{1/2}$ of 0.852 V, underscoring its efficacy. For the OER, the LaPNC catalyst showcased substantially reduced overpotentials of 262 mV and 431 mV at respective current densities of 10 and 100 mA cm^{-2} (Fig. 6d and e). LaPNC achieved a remarkable peak power density of 202 mW cm^{-2} (Fig. 6g and h) while maintaining an outstanding charge–discharge efficiency of 95.4% after 20 hours of continuous operation. Lu *et al.* devised an ingenious zinc-assisted MgO templating strategy to construct a hierarchical porous structure rich in $Fe–N_4$ active sites.[69] During synthesis, zinc species effectively isolate Fe atoms and subsequently volatilize at high temperatures to form micropores, while removing the MgO template generates meso- and macropores. This unique approach prevents Fe atom aggregation and creates a multi-level pore network conducive to reactant diffusion. Nitrogen adsorption–desorption isotherms delineated the catalyst's extraordinarily elevated specific surface area, quantified at 1061.45 m^2 g^{-1}. The Fe–N–C catalyst demonstrated superlative ORR efficacy, attaining a notable $E_{1/2}$ of 0.895 V. Within a functional ZAB, the catalyst maintained a formidable power density peak of mW cm^{-2} and upheld robust operational stability throughout an extended 643-hour cycling assay.

Another extensively employed template technique is the soft template method, which utilizes organic molecules or polymers, such as surfactants and block copolymers, as external templates. The ordered architectures generated through self-assembly or phase separation guide the synthesis of porous carbon materials. Wu *et al.* used a soft template-directed interlayer confinement synthesis method, and amphiphilic molecules such as perfluorotetradecanoic acid (PFTA) and stearic acid (SA) self-assemble to form two-dimensional layered micelles serving as soft templates.[91] Fe and Co single atoms are anchored within the interlayers of these templates. Subsequently, a trilayer sandwich structure is created by coating with polypyrrole (Ppy), followed by high-temperature thermal treatment, resulting in structurally stable 3D porous Fe–Co DSACs (Fig. 7a and b). The $E_{1/2}$ reaches 0.86 V (Fig. 7c), and ZABs based on Fe–Co DSACs exhibit an open-circuit voltage of 1.51 V. Additionally, these batteries achieve a specific capacity of 782.1 mA h g_{Zn}^{-1} and a maximum power density of 152.8 mW cm^{-2} (Fig. 7d).

The self-templating method leverages the intrinsic composition or structure of materials to spontaneously form porous structures under specific conditions, without the need for external templates. This process involves internal reorganization or decomposition, leading to the autonomous development of the desired porous architecture. Liu *et al.* employed Bio-MOF-1 as a template and introduced Co^{2+} into the pores *via* an ion exchange strategy, resulting in generation of numerous mesopores.[93] Subsequent high-temperature pyrolysis converted the organic ligands into porous carbon with excellent conductivity, while the cobalt metal centers were transformed into ultra-small cobalt nanoparticles, yielding Co@N-HPC-800. In ORR testing, this catalyst exhibited an $E_{1/2}$ of 0.82 V and an overpotential of 1.69 V. The assembled ZAB demonstrated a specific capacity of 129 mA h g^{-1} and a peak power density of 89.1 mW cm^{-2}. Remarkably, after 150 consecutive discharge–charge cycles, the battery voltage remained nearly unchanged, highlighting its exceptional stability. Furthermore, self-templates can play multifaceted roles. For instance, Gong *et al.* synthesized highly ordered, uniformly distributed Fe_2O_3 nanorods through the oxidation of Fe-MIL-88B under atmospheric conditions (Fig. 7e).[92] These nanorods provide Fe^{3+} to facilitate the polymerization of polypyrrole and serve as a scaffold promoting one-dimensional polymer growth. The strategy employed involved *in situ* polymerization followed by a thermal treatment process, during which the iron from the Fe_2O_3 nanorods was homogeneously incorporated into the resultant carbon matrix, synergistically engaging with nitrogen to yield Fe/N-CNR catalysts. Characterized by $Fe–N_4$ configuration, these catalysts demonstrated remarkable catalytic prowess, evidenced by an $E_{1/2}$ of 0.90 V, achieving a peak power density of 181.8 mW cm^{-2} and an exceptional specific capacity of 998.67 W h kg^{-1} (Fig. 7f–h).

3.2.2. Self-assembly method. The self-assembly approach leverages the inherent ability of molecules or nanoparticles to spontaneously organize into ordered structures under specific conditions, facilitating the precise synthesis of porous carbon materials. This technique affords meticulous control over pore size, channel arrangement, and overall architecture. The resultant self-assembled porous carbons exhibit exceptionally high surface areas and superior physicochemical properties, rendering them highly effective in diverse applications such as electrochemical energy storage, catalysis, and adsorption. Chang *et al.* utilized a straightforward self-assembly and calcination approach (Fig. 8a), and a 3D N/P/S-doped carbon nanoflower structure (Co/SP-NC) containing highly branched carbon nanotubes was successfully synthesized.[94] SEM and TEM analyses have confirmed the distinctive nanoflower morphology and the highly branched architecture of the carbon nanotubes (Fig. 8b and c). The Co/SP-NC sample boasts a specific surface area of 521.9 m^2 g^{-1} (Fig. 8d), featuring the profusion of micropores and mesopores. These micropores serve as active sites for catalytic reactions, significantly enhancing catalytic efficiency. In terms of electrochemical performance, the Co/SP-NC catalyst exhibits exceptional bifunctionality in the ORR and

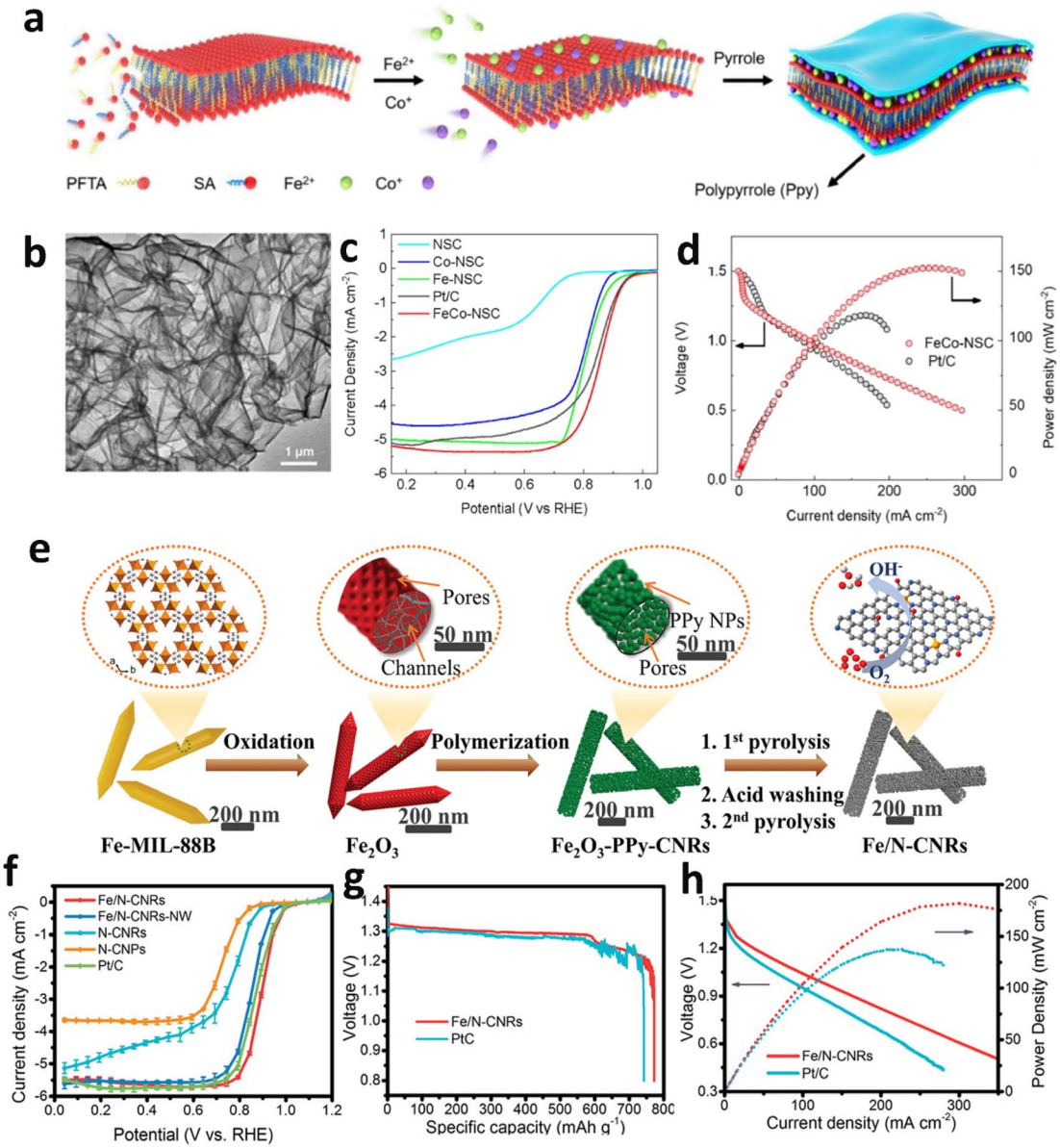

Fig. 7 (a) Synthesis steps for FeCo-NSC. (b) TEM details of FeCo-NSC. (c) LSV curves of FeCo-NSC and comparative samples. (d) Polarization and power density of ZABs with FeCo-NSC and Pt/C. Reproduced with permission from ref. 91 Copyright 2023, Elsevier. (e) Diagrammatic representation of the fabrication steps for Fe/N-CNRs. (f) LSV curves for Fe/N-CNRs and other samples. Comparative analysis of specific capacity (g) and voltage and power output performance (h) for Fe/N-CNRs and Pt/C electrodes in ZABs at a discharge current of 10 mA cm^{-2} and across various current densities. Reproduced with permission from ref. 92 Copyright 2021 Wiley-VCH.

OER. The catalyst achieved an $E_{1/2}$ of 0.8603 V and registered an overpotential of 343 mV at 10 mA cm^{-2} (Fig. 8e and f), substantiating its robust catalytic proficiency in the ORR and OER. Furthermore, ZAB incorporating Co/SP-NC as the active electrode material exhibited a significant specific capacity of 801 mA h g_{Zn}^{-1} at the same current density and maintained exceptional cycling stability across 280 hours with negligible performance decay (Fig. 8g and h). The assembly employing Co/SP-NC realized a peak power density of 187 mW cm^{-2} (Fig. 8i). Han *et al.* employed a refined electrochemical exfoliation technique to fabricate graphene sheets with tailored oxygen content by modulating the oxidation conditions.[95] The ZABs leveraging porous curved graphene film (PCGF) technology manifested a peak power density of 329 mW cm^{-2} and an energy density of 967.46 W h kg^{-1}. Furthermore, Wagh *et al.* expertly engineered a 3D, flexible, self-supporting membrane catalyst, composed of intricately woven supramolecular polymers and nitrogen-deficient carbon nitride nanotubes (PEMAC@NDCN), utilizing a sophisticated self-assembly method.[96] This catalyst exhibited an extraordinary power density of 211 mW cm^{-2} and an impressive energy density of 1056 W h kg^{-1}. Moreover, at 50 mA cm^{-2}, it sustained a cycle life surpassing 2580 cycles. Different assembly methods can produce various morphologies of metal anchor points. Shu *et al.*

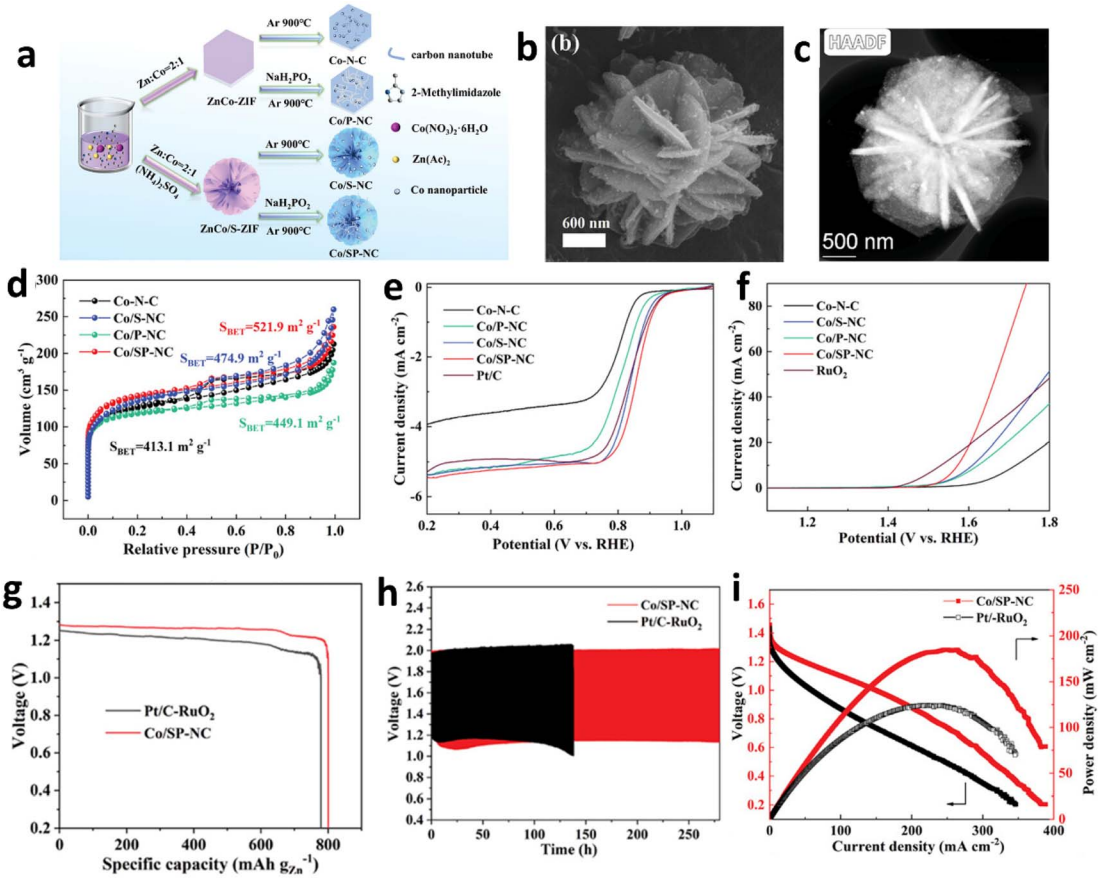

Fig. 8 (a) Schematic representation of the synthesis process for 3D self-assembled Co/SP-NC nanoflowers with highly branched carbon nanotubes. SEM images (b) and HAADF-STEM image (c) of Co/SP-NC. (d) N_2 adsorption/desorption isotherms for Co/SP-NC and comparative samples. LSV curves for the ORR (e) and OER (f). Comparative analysis of specific capacities (g), stability evaluation through galvanostatic cycling (h), and electrochemical discharge profiles with associated power density (i) characteristics for ZABs using Co/SP-NC and Pt/C–RuO_2 electrodes.[94] Reproduced with permission from ref. 94 Copyright 2023 Wiley-VCH.

used a chitosan and folic acid self-assembled composite to provide metal ion anchoring sites, resulting in CoCNTs/PNAs. In ORR tests, this material exhibited a high $E_{1/2}$ of 0.925 V, a low overpotential of 1.539 V in the OER, and a maximum power density of 371.6 mW cm^{-2} in ZAB tests.[97]

3.2.3. Sol–gel method. The sol–gel approach facilitates a transition from a dispersed particulate system (sol) to an integrated 3D network (gel) through a meticulous chemical synthesis process. By meticulously tuning the reaction conditions, such as pH, temperature, and the concentration of precursors, the microstructures of the catalyst can be precisely manipulated. Within ZABs, the sol–gel process produces porous carbon materials encompassing a broad spectrum of active sites. These structures significantly enhance the diffusion dynamics of gases and electrolytes, thereby substantially augmenting the overall performance of the batteries.

For example, Zhu and colleagues ingeniously synthesized a single-atom catalyst, FeZ–N/$S_{0.6}$–C, through a multistage process starting with the integration of $[Fe(phen)_3]^{3+}$, $ZnCl_2$, and polyacrylamide (PAM).[79] This mixture underwent a free-radical polymerization reaction, catalyzed by ammonium persulfate, leading to gel precursor formation (Fig. 9a). Subsequent high-temperature pyrolysis of this precursor yielded the catalyst, distinguished by its well-defined pore structure (Fig. 9b). This catalyst demonstrated remarkable electrochemical properties in ZABs, achieving an exceptionally high $E_{1/2}$ of 0.93 V (Fig. 9c). Furthermore, it exhibited superior performance metrics, with a specific capacity of 816.0 mA h g_{Zn}^{-1} and a peak power density of 76.3 mW cm^{-2} (Fig. 9d and e), underscoring its potential for enhancing battery efficiency. The sol–gel method provides a robust technique for anchoring targeted metals onto specifically designed carriers. Cui *et al.* utilized the sol–gel method to anchor ruthenium on activated carbon spheres, initially mixing $RuCl_3$ with urea to form a uniform sol.[80] High-temperature calcination develops the Ru–N structure and removes organic components, resulting in Ru–SAs@N-ACSs. In ORR tests, this catalyst achieved an $E_{1/2}$ 0.87 V and exhibited a peak power density of 179 mW cm^{-2} in ZABs. Wang *et al.* employed iota-carrageenan and NiCo-MOF hydrogels as precursors to synthesize hierarchically porous Ni_3S_2–Co_9S_8/carbon aerogels.[98] These aerogels were subjected to carbonate under a nitrogen atmosphere, leading to Ni_3S_2 and Co_9S_8 sulfides embedded within a carbon matrix, producing Ni_3S_2–Co_9S_8/NCA. In OER tests, the material achieved a low

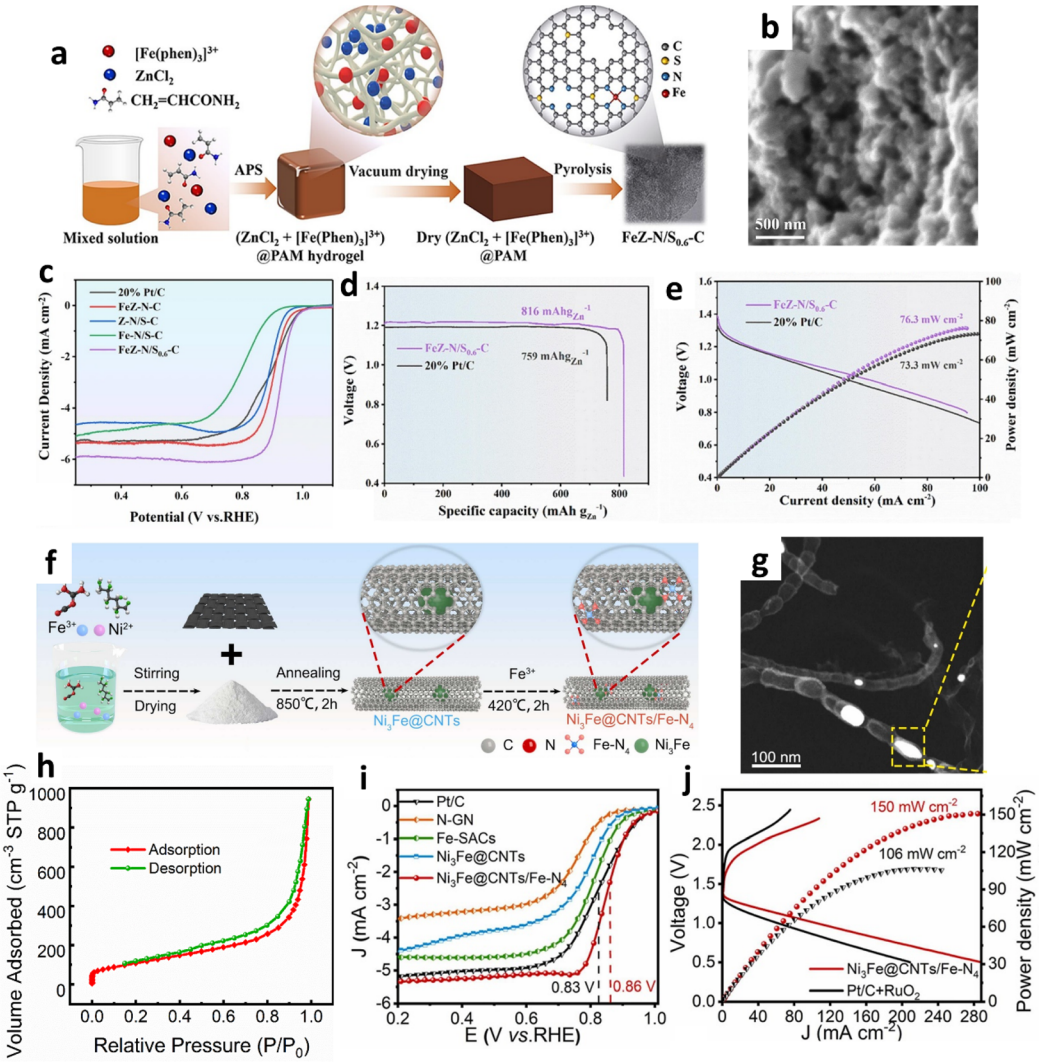

Fig. 9 (a) Synthesis process for FeZ–N/$S_{0.6}$–C. (b) High-resolution SEM characterization of FeZ–N/$S_{0.6}$–C. (c) LSV curves for FeZ–N/$S_{0.6}$–C and comparative samples. (d) Constant current discharge profiles for aqueous ZABs operated at 20 mA cm^{-2}. (e) Polarization and power density response of quasi-solid ZABs with FeZ–N/$S_{0.6}$–C and 20% Pt/C electrodes. Reproduced with permission from ref. 79 Copyright 2024, Elsevier. (f) Synthesis diagram of Ni_3Fe@CNTs/Fe–N_4. (g) TEM images of Ni_3Fe@CNTs/Fe–N_4. (h) Adsorption–desorption curves of nitrogen on Ni_3-Fe@CNTs/Fe–N_4. (i) ORR electrochemical profiles for various catalysts in O_2-saturated 0.1 M KOH. (j) Power profiles for ZABs using Ni_3Fe@CNTs/Fe–N_4 and Pt/C + RuO_2.[87] Reproduced with permission from ref. 87 Copyright 2024, Elsevier.

overpotential of 337 mV and demonstrated a high power density of 256 mW cm^{-2}.

3.2.4. CVD method. The utilization of CVD has been pivotal in constructing diverse carbon-based nanocatalysts, notably carbon nanotubes and graphene. This advanced technique involves the directed flow and meticulous deposition of vapor-phase precursors onto carefully selected substrates or patterns. Zhang *et al.* by employing CVD within an argon milieu, synthesized a composite catalyst composed of Ni_3Fe nanoalloys and Fe–N_4 sites integrated within carbon nanotubes (Ni_3-Fe@CNTs/Fe–N_4) (Fig. 9f and g).[87] This catalyst, featuring a mesopore diameter of approximately 2.3 nanometers and an expansive specific surface area reaching 705.65 m^2 g^{-1} (Fig. 9h), demonstrated prodigious catalytic prowess. Consequently, the constructed primary ZAB achieved a peak power density of 150 mW cm^{-2} (Fig. 9j) and exhibited robust operational durability over 307 hours in an alkaline environment. Moreover, the Ni_3-Fe@CNTs/Fe–N_4 catalyst displayed an ORR $E_{1/2}$ of 0.86 V in 0.1 M KOH solution (Fig. 9i), affirming its performance on par with conventional Pt/C catalysts.

3.2.5. Chemical etching method. Compared to the "one-pot" method, the chemical etching approach is an economical, efficient, and straightforward strategy for large-scale synthesizing porous carbon catalysts. Inorganic acids and organic solvents are the representative pore-forming chemical etching agents, such as HF acid that can serve in desilication for porous carbon catalyst formation. Zhang *et al.* reported a HF acid etching SBA-15 hard template strategy to synthesize ordered mesoporous carbon substrates,[99] and Dou *et al.* reported a HF acid etching SiO_2 gel composite strategy to synthesize macro/

meso/microporous Fe/N/P-codoped hollow catalysts.[100] These methods demonstrate that the chemical etching strategy can modify porous catalysts with specific structures *via* template agent selection. For organic agents, Yu *et al.* adopted the *N*,*N*-dimethylformamide (DMF)-assisted solvothermal etching strategy to convert NiFe Prussian blue analog nanoboxes with hollow structures and dual vacancies.[101]

This chapter meticulously explores various synthesis techniques applied in porous carbon materials. These methodologies augment materials' specific surface area and refine the pore dimensions and their distribution. Consequently, these adjustments directly impact the electrochemical activity and the comprehensive performance of the batteries. Researchers can design porous carbon materials with tailored functionalities through advanced synthesis methods. As our understanding of these synthesis techniques deepens, future research may further explore how to precisely control the properties of catalytic sites through these methods, aiming to achieve more efficient and sustainable battery systems.

4. Adjustment of catalytic sites

4.1. Heteroatom-enhanced ZAB dynamics

In the pursuit of optimizing electrocatalytic activity for the ORR, the strategy of metal-free heteroatom doping, specifically nitrogen (N), boron (B), sulfur (S), oxygen (O), and phosphorus (P) into carbon matrices has been identified as a promising avenue.[102–107] This approach aims to modify the electronic and spin distribution within the sp^2 carbon framework, thereby enhancing the effectiveness of catalytic sites. N-doped carbon materials can improve the electronic properties of nearby carbon atoms and then impact the adsorption behaviors of intermediary substances.[108] This effect is attributed to the superior electronegativity of nitrogen-doped sites relative to traditional carbon sites. The development of nitrogen-doped carbon-based electrocatalysts for the ORR originated with the pioneering work by the Dai group in 2009, which unveiled an efficient nitrogen-doped carbon nanotube catalyst.[109] Subsequent investigations have expanded a variety of nitrogen configurations within these catalysts, including graphitic, pyrrolic, oxidic, triazinic, and sp-hybridized nitrogen forms.[110] It has been observed that the catalytic efficiency for the ORR of these nitrogen forms decreases in the following order: pyridinic N, pyrrolic N, graphitic N, and oxidized N, underscoring a complex interplay between the type of nitrogen doping and the resulting catalytic performance.[111–114] Despite the concurrent presence of various nitrogen species within doped catalysts complicating the attribution of specific catalytic roles, extensive investigations into diverse nitrogen-doped carbon structures-ranging from CNTs and graphene to graphitic arrays and carbon nitride (C_3N_4)-based materials have underscored their potential in ORR applications.[115,116]

Furthermore, such as B, S, O, and P alongside N, are widely recognized as a metal-free heteroatom-doping strategy for boosting the ORR process due to their synergistic effects.[117,118] Incorporating these metal-free heteroatoms into the carbon matrix can redistribute the electronic structure and spin-charge densities, promoting electron density accumulation of heteroatom-C active sites, thereby accelerating O-contained intermediate conversion during the ORR and OER. These heteroatom-N active sites include N/S-, B/N-, N/P-, N/F-, and P/C_3N_4.[119–123] For instance, Ding and colleagues devised a catalyst characterized by a thin, porous nanosheet architecture, composed of N and S co-doped carbon, synthesized utilizing S-g-C_3N_4 and P123 as precursors (Fig. 10a).[119] Raman spectroscopy analyses revealed an elevated defect density, attributable to significant sulfur incorporation (Fig. 10b). DFT calculations illustrated that sulfur integration into nitrogen-doped graphene sheets enhances the charge density of the carbon atoms, rendering them more electropositive. Furthermore, this sulfur doping modifies the electronic configuration of the carbon atoms, increasing both their charge and spin densities, which significantly improves the chemical adsorption capabilities for oxygen molecules and the efficacious cleavage of the O–O bond (Fig. 10e). This alteration augments their electron affinity and facilitates their participation in the ORR, achieving a notable $E_{1/2}$ of 0.863 V (Fig. 10c). The ZAB utilizing the N–S–C-2 catalyst reached a peak power density of 86 mW cm^{-2} (Fig. 10d). Su *et al.* harnessed high-temperature pyrolysis employing a BF_4-containing precursor to introduce nitrogen, boron, and fluorine simultaneously into carbon matrices.[124] This innovative ternary doping approach not only refines the electronic architecture of the material but also bolsters the adsorption capabilities of oxygen molecules at the catalytic sites. Notably, the active sites incorporate pyridinic nitrogen, boron, and fluorine, emerging as efficacious agents for the ORR. These sites prompt a redistribution of electrons (Fig. 10h), thus decreasing the ORR overpotential and substantially enhancing the catalyst's overall efficacy. This led to an elevated $E_{1/2}$ of 0.858 V (Fig. 10f). The DFT calculations have delineated that *O transformation constitutes the potential-determining step (Fig. 10g), featuring a comparatively modest alteration in Gibbs free energy. While NC catalysts demonstrate commendable efficacy in the ORR, their deployment in rechargeable ZABs is constrained due to their lackluster performance in the OER (Table 2).

4.2. Single-atom enhancements for ZABs

Apart from centers doped solely with heteroatoms, single-atom catalysts anchored on carbon substrates emerge as powerful alternatives for the ORR in zinc–air batteries, celebrated for their remarkable intrinsic efficacy and outstanding efficiency at the atomic level. Currently, the most intensely studied and potent single-atom catalysts for ZABs include those with Fe, Co, Cu, and Mn all stabilized on nitrogen-doped carbon matrices.[143–158] Particularly distinguished are Fe–N_4 and Co–N_4 sites, which exhibit the highest activity for the ORR in alkaline media.[159–163] Their performance in catalyzing ZABs is on par with or exceeds that of conventional Pt/C catalysts. Zuo *et al.*[159] employed a synthesis strategy utilizing pyridyl-conjugated microporous polymer precursors to fabricate FeN_4–C catalysts, which achieved an $E_{1/2}$ of up to 0.89 V (Fig. 11c). HAADF-STEM imaging elucidated the homogeneous dispersion of Fe atoms within the carbon matrix (Fig. 11a). EXAFS spectroscopy

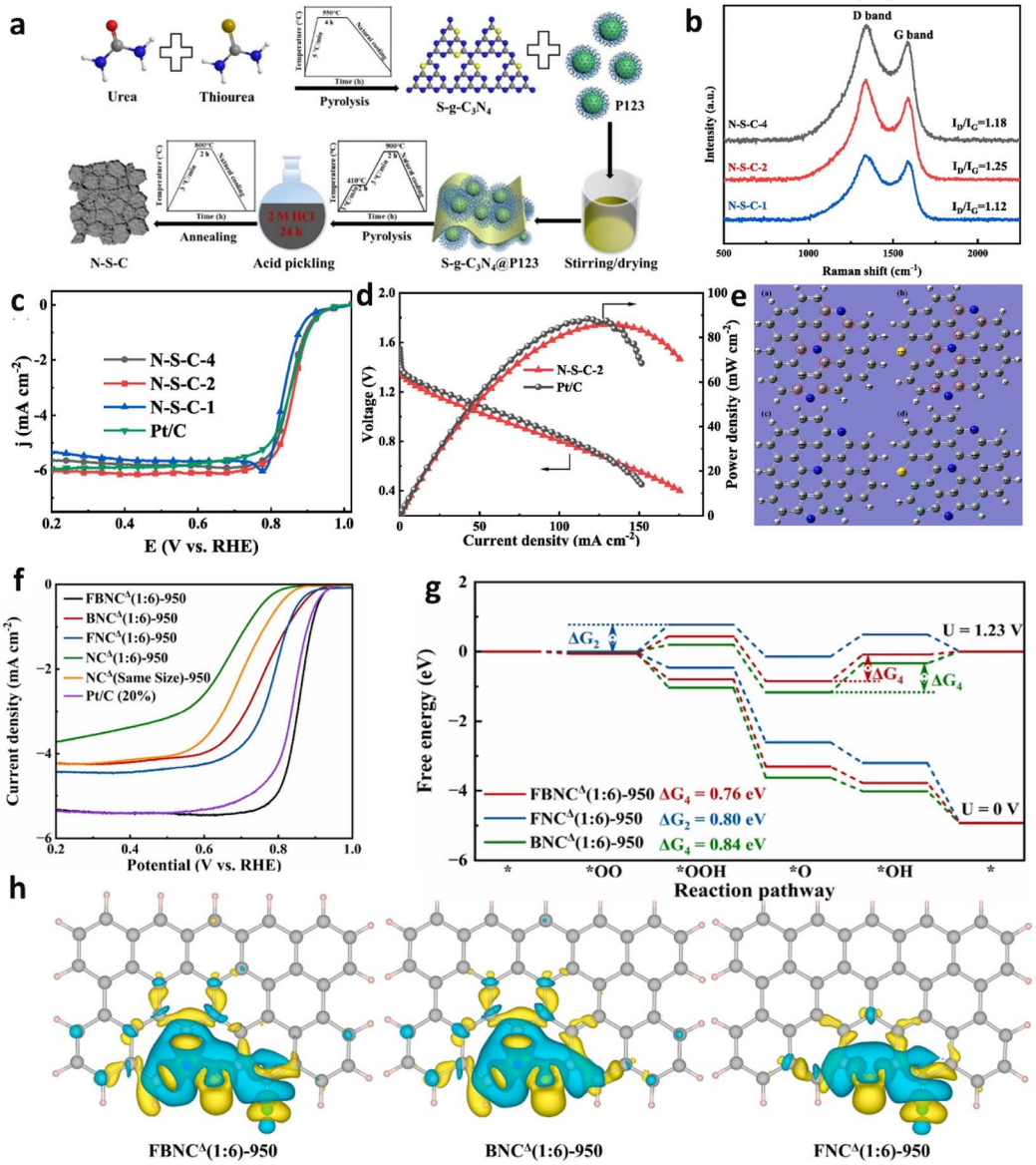

Fig. 10 (a) Diagram depicting the synthesis procedure for N–S–C. (b) Raman spectra of N–S–C catalysts. (c) ORR polarization curves of N–S–C variants and Pt/C catalysts. (d) Voltage and power performance curves of N–S–C-2 and Pt/C catalysts in ZABs under varying load conditions. (e) Charge and spin density mappings for nitrogen-doped and N–S co-doped graphene sheets. Reproduced with permission from ref. 119 Copyright 2022, Elsevier. (f) LSV curves. (g) ORR pathways. (h) Illustration of charge density variations across diverse doped configurations. Reproduced with permission from ref. 124 Copyright 2024, Elsevier.

revealed a pronounced peak at 1.5 Å (Fig. 11b), indicative of Fe–N or Fe–O coordination, thus substantiating the presence of Fe atoms within the FeN_4 structure. Charge density difference and Bader charge analyses demonstrated that the metal centers in the Fe–Fe-0.23 nm model exhibited minimal charge depletion (Fig. 11d), resulting in the weakest *OH adsorption energy (Fig. 11e). The dual single-atom catalyst, leveraging synergistic effects and electronic structure modulation, augmented ORR efficiency and ameliorated suboptimal OER performance. Gu *et al.* employed a hydrothermal–pyrolysis approach, adjusting Fe and Co precursor ratios to synthesize a series of Fe_xCo_y-NC catalysts.[164] AC-HAADF-STEM imaging revealed numerous bright spots uniformly dispersed across the nitrogen-doped carbon matrix (Fig. 11f), indicating homogeneous Fe and Co single atom distribution. X-ray photoelectron spectroscopy (XPS) analysis further substantiated the existence of Fe/Co–N coordination (Fig. 11g). These catalysts demonstrated a remarkable $E_{1/2}$ of up to 0.893 V and an overpotential of just 343 mV for the OER (Fig. 11h and i). DFT calculations illustrated the underlying mechanisms, showcasing the synergistic interaction between the Fe–Co dual sites on the nitrogen-doped carbon matrix. The adjacent configuration of Fe–N_4 and Co–N_4 sites facilitated stronger hybridization between the Co (d_{z^2}) and OO* (p_x, p_z) electronic orbitals, enhancing the O_2 activation capability at the Co-active sites.

Table 2 Comparative analysis of porous carbon–oxygen catalysts in ZABs, focusing on their performance in the ORR/OER with configurations including metal-free heteroatoms, single metal atoms, and sites comprising metal alloys and compounds

Catalytic site	Catalyst material	ORR ($E_{1/2}$, V)	OER ($E_{j=10}$, V)	Power density (mW cm^{-2})	Specific capacity (mA h g_{Zn}^{-1})	Stability (mA cm^{-2}@h/cycle)	References
Metal-free heteroatoms	JCNT-0.5	0.88	—	142	818	20@1.94 h	125
	NBCNT-10	0.82	1.53	173.93	—	10@12 h	102
	mf-pClNC	0.91	—	276.88	1203.2	20@200 h	126
	F-NPC	0.86	1.65	206.3	862.1	10@500 cycles	123
	NHCF-900	0.89	1.49	204.8	804.7	2@350 h	127
Single metals	CNT@CoSA-Co/NCP	0.87	1.61	172	864.8	5@210 h	128
	SAFe-SWCNT	0.93	1.6	210	772	20@33.3 h	129
	Pt/NBF-ReS_2/Mo_2CT_x	0.911	1.564	180.2	786	10@100 h	130
	FeCo-NSC	0.86	—	152.8	782.1	20@120 h	91
	Fe(Cd)–CN_x	0.905	—	170.8	800.6	5@600 h	131
	Fe SA/NCZ	0.87	1.55	101	—	2@44 h	132
	Ni,Fe-DSAs/NCs	0.895	1.612	217.5	780.1	40@110 h	133
	FeSA/N-PSCS	0.87	1.612	164.5	725.3	10@150 h	134
	Co-FNC	0.9	1.476	246	817	10@100 h	135
	SD-Fe-N/C	0.852	1.565	213	800	10@300 cycles	136
	SC-CuSA-NC	0.83	1.544	124.9	775	10@55 h	137
Metal alloys and compounds	FeCo-NC@Co_2P-NC	0.862	1.536	159.3	881.3	10@280 cycles	138
	CoFe/N-HCSs	0.791	1.522	96.5	777.4	5@160 h	139
	CoFe/Fe_2N@N-CNTs	0.89	1.556	173	846	10@1000 h	140
	$FeNi_3$@NC	0.782	1.521	149.7	658	10@280 h	141
	H-NiFe/CNF	0.833	1.504	238.1	790.2	5@800 cycles	142

Building on this foundation, integrating heteroatoms such as phosphorus, sulfur, and oxygen into M–N_x/C catalyst frameworks can significantly enhance OER and ORR efficacies. Chen *et al.* investigated an SA-Fe-SNC@900 catalyst, where metal atoms coordinate with a carbon–nitrogen matrix, forming single-atom dispersed M–N_4–S active sites.[165] DFT investigations have uncovered the nuanced influence of sulfur doping in refining the electronic framework and amplifying the catalytic efficiency at Fe–N_4 sites. S addition has been pivotal in fine-tuning the adsorption dynamics of intermediates, effectively reducing the energy barriers associated with the ORR. Notably, Fe–N_4 centers enriched with sulfur display increased electron density, which elevates the catalytic capabilities (Fig. 11j and k).

4.3. Alloyed metals for enhanced oxygen catalysis

Carbon-supported metal compounds have been employed as effective catalysts for enhancing bifunctional activity in the ORR and OER. The synergistic combination of carbon with metal alloys/compounds increases active sites, conductivity, and durability.[166–170] Research has extensively investigated carbon-supported sulfides, carbides, nitrides, and phosphides, demonstrating their efficacy in advancing rechargeable ZAB performance. FeCo nucleus-bound carbon skeletons (FeCo-MI@TAP-900) were successfully synthesized *via* an innovative *in situ* spatial-embedding strategy.[171–178] The abundant FeCo nanoparticles derived from MOFs are encapsulated within a 3D porous carbon framework derived from POPs, effectively preventing the aggregation and leaching of nanoparticles during electrochemical reactions. Empirical analyses have elucidated that FeCo-MI@TAP-900 possesses a specific surface area of 228.93 m^{-2} g^{-1} alongside a pore volume of 0.22 cm^3 g^{-1}, illustrating the coexistence of micro- and mesopores optimal for electrocatalytic processes. In the realm of electrochemical efficacy, FeCo-MI@TAP-900 is distinguished by its exceptional catalytic prowess. Specifically, it registers an $E_{1/2}$ of 0.860 V for the ORR and an overpotential of 1.615 V at 10 mA cm^{-2} for the OER, surpassing the capabilities of many established catalysts. Within practical deployments, the ZAB utilizing FeCo-MI@TAP-900 achieves an open-circuit voltage of 1.51 V. Moreover, this battery configuration demonstrates extraordinary stability across extended operational durations, maintaining consistent performance after 2100 charge–discharge cycles. Under rigorous operational conditions, specifically high-load scenarios, the battery featuring FeCo-MI@TAP-900 exhibits a robust power density of 118 mW cm^{-2} and a significant specific capacity of 805 mA h g_{Zn}^{-1}. The synergistic interaction among various alloys furnishes multiple active sites, enhancing the catalytic efficiency. Recently, Jang *et al.* engineered a groundbreaking bifunctional catalyst, termed 3D graphene-coated metal catalyst (3d-GMC), by synthesizing few-layer graphene *in situ* on a 3D nitrogen-doped carbon scaffold embedded with transition metal alloys such as CoNi, FeNi, and CoFe (Fig. 12a and b).[179] The strategic *in situ* generation of few-layer graphene atop these alloy surfaces not only augmented the specific surface area of the 3d-GMC to 211.19 m^2 g^{-1} (Fig. 12c) but also significantly boosted its electrical conductivity and corrosion resistance, attributable to the synergistic interactions between the graphene and the transition metal alloys. The catalyst sustained its performance robustly for 83 hours at 10 mA cm^{-2} (Fig. 12d). In practical deployments within ZABs, the 3d-GMC demonstrated a remarkable specific power density of approximately 100 mW cm^{-2} and maintained its structural and

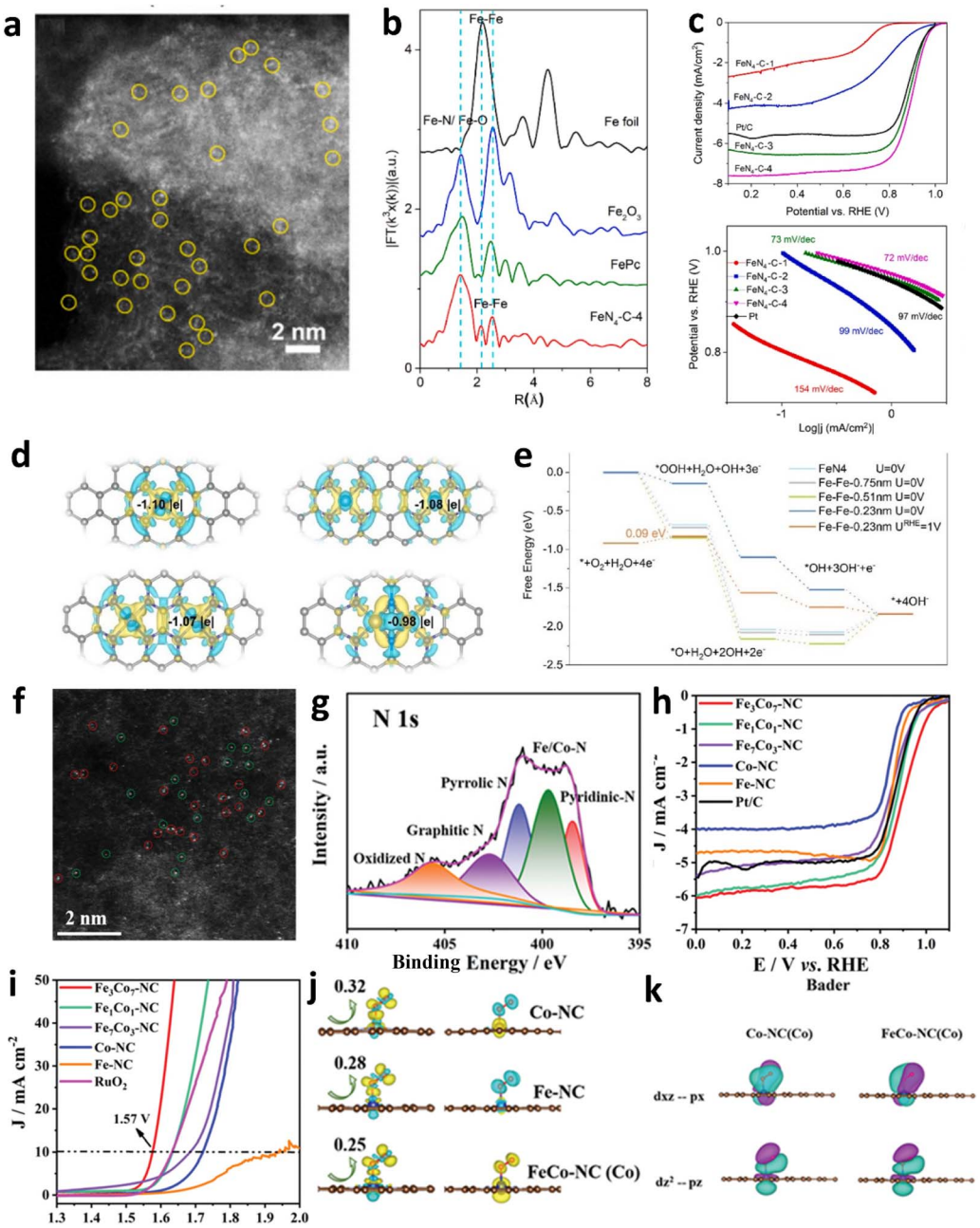

Fig. 11 (a) High-resolution HAADF image of the FeN_4–C material's single-atom structure. (b) EXAFS spectra of various iron-based materials. (c) Polarization curves and Tafel plots for FeN_4–C catalysts in the ORR. (d) Charge density differences in FeN_4 and Fe–Fe dimers at various distances. (e) Free energy profiles for the ORR on FeN4 and Fe–Fe dimers with varying separations. Reproduced with permission from ref. 159 Copyright 2023, Elsevier. (f) HAADF-STEM images of Fe_3Co_7-NC. (g) XPS spectra of N 1s. (h) ORR polarization curves of Fe_3Co_7-NC and other catalysts. ORR (h) and OER (i) polarization curves for Fe_3Co_7-NC, various binary metal-NCs, and Pt/C or RuO_2. (j) Charge density difference and spin density. (k) Maximally localized Wannier functions of Co $3d_{xz}$ ($3d_{z^2}$) and O_2 $2p_x$ ($2p_z$) orbitals. Reproduced with permission from ref. 164 Copyright 2022 Wiley-VCH.

functional integrity over 200 hours of continuous charge–discharge cycles (Fig. 12e).

Furthermore, carbides and nitrides, characterized by their exceptional electrical conductivity and corrosion resistance, have been rigorously explored as highly promising electrocatalysts for the ORR. Liu *et al.* by utilizing an innovative synthesis strategy that merges electrospinning with high-temperature calcination, adeptly loaded FeC, FeN, and MnO nanoparticles onto carbon nanofibers (CNFs) to synthesize Fe_4Mn_4-NC-800, optimizing exposure of highly active sites.[180] TEM and HRTEM analyses confirm that the catalyst's nanoparticles, each approximately 20 nm, are uniformly distributed within the carbon fibers, which measure about 300 nanometers in diameter. BET analysis indicates that the catalyst possesses

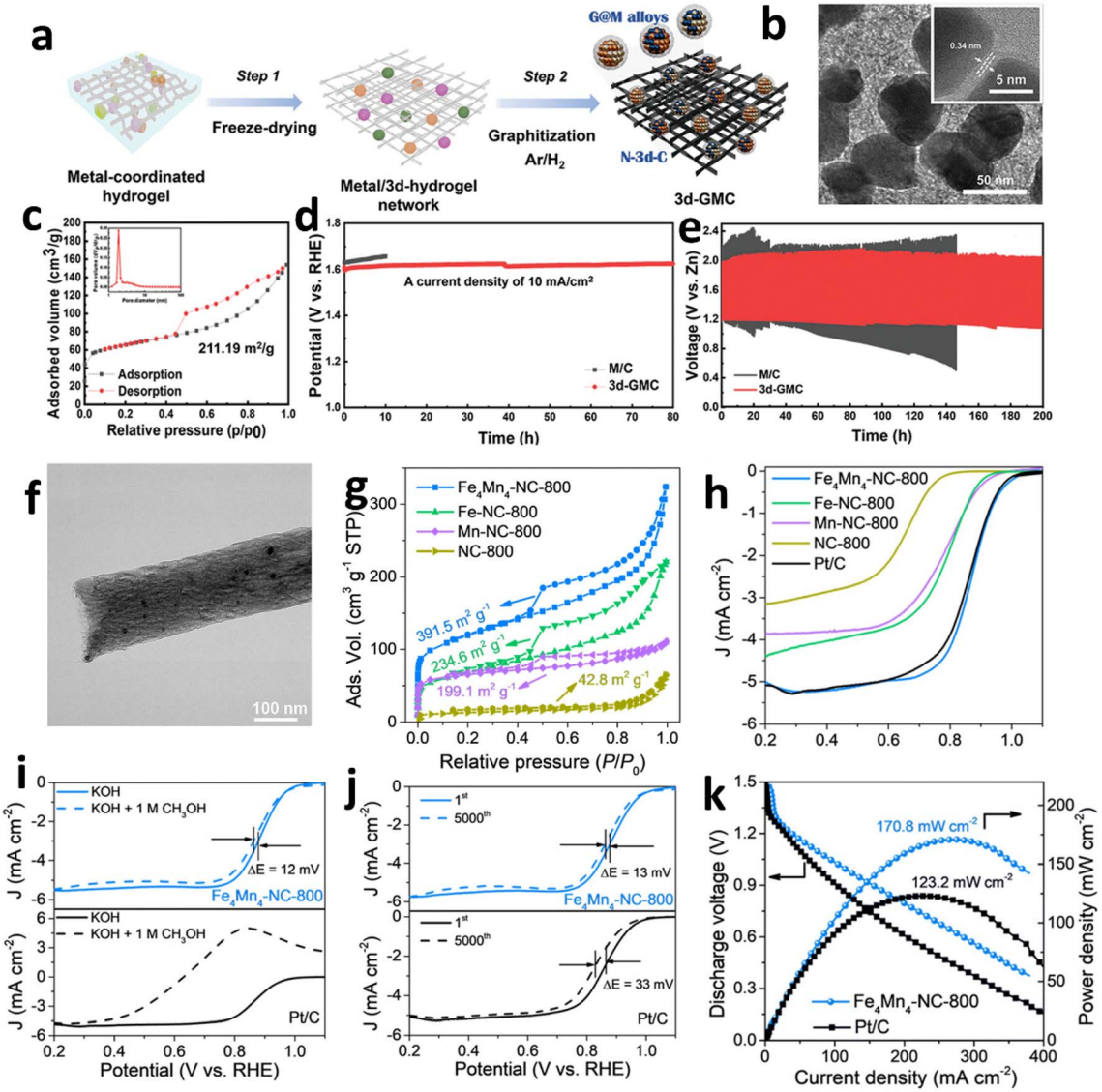

Fig. 12 (a) Schematic diagram of the simple process for preparing a 3D-GMC using metal-coordinated hydrogels. (b) TEM image of the 3d-GMC. (c) N_2 adsorption/desorption isotherm for the 3d-GMC. (d) Durability test comparing the performance of M/C (black) and the 3d-GMC (red). (e) Cyclability comparison of ZABs with the 3d-GMC cathode (red) and commercial zinc foil anode *versus* those with the M/C cathode (black). Reproduced with permission from ref. 179 Copyright 2023 Wiley-VCH. (f) TEM image of Fe_4Mn_4-NC-800. (g) N_2 adsorption/desorption isotherms of Fe_4Mn_4-NC-800, Fe-NC-800, Mn-NC-800, and NC-800. (h) ORR LSV curves of Fe_4Mn_4-NC-800 compared with those of other catalysts. The methanol crossover tests (i) of Fe_4Mn_4-NC-800 and (j) Pt/C over 5000 cycles. (k) Specific power *versus* current density for ZABs with Fe_4Mn_4-NC-800 and Pt/C. Reproduced with permission from ref. 180 Copyright 2023 Royal Society of Chemistry.

a specific surface area of 391.5 $m^2\ g^{-1}$ and features a rich array of mesoporous structures with an average pore size of approximately 4 nm (Fig. 12f and g). Fe_4Mn_4-NC-800 exhibits an onset potential of 1.06 V and an $E_{1/2}$ of 0.86 V (Fig. 12h). This catalyst demonstrates remarkable methanol resistance, evidenced by a mere 12 mV negative shift in a 1.0 M methanol environment. Stability tests were conducted through 5000 cycles and only a 13 mV minimal negative shift in the $E_{1/2}$ was observed (Fig. 12i and j). Employed as the cathode material in ZABs, Fe_4Mn_4-NC-800 enables a remarkable open-circuit voltage of up to 1.51 V, a specific capacity of approximately 793 mA h g_{Zn}^{-1}, and a power density of 170.8 mW cm^{-2} (Fig. 12k).

4.4. Metal oxides for enhanced oxygen catalysis

Furthermore, oxides/hydroxides are promising alternatives to precious metal-based catalysts for bifunctional ZAB catalysts.[181–187] Chang *et al.* ingeniously engineered vertically oriented layered double hydroxide (LDH) nanosheets on hollow carbon nanoframes (Co@NC) *via* a metal-oxide-assisted synthesis technique (Fig. 13a and b).[182] Denoted as Co@NC@LDHs, it showcased outstanding bifunctional electrocatalytic efficiency. It demonstrated a low overpotential of 330 mV for the OER at 10 mA cm^{-2} and an impressive $E_{1/2}$ of 0.88 V for the ORR (Fig. 13c and d). Furthermore, a ZAB incorporating Co@NC@LDHs as the electrocatalyst achieved an

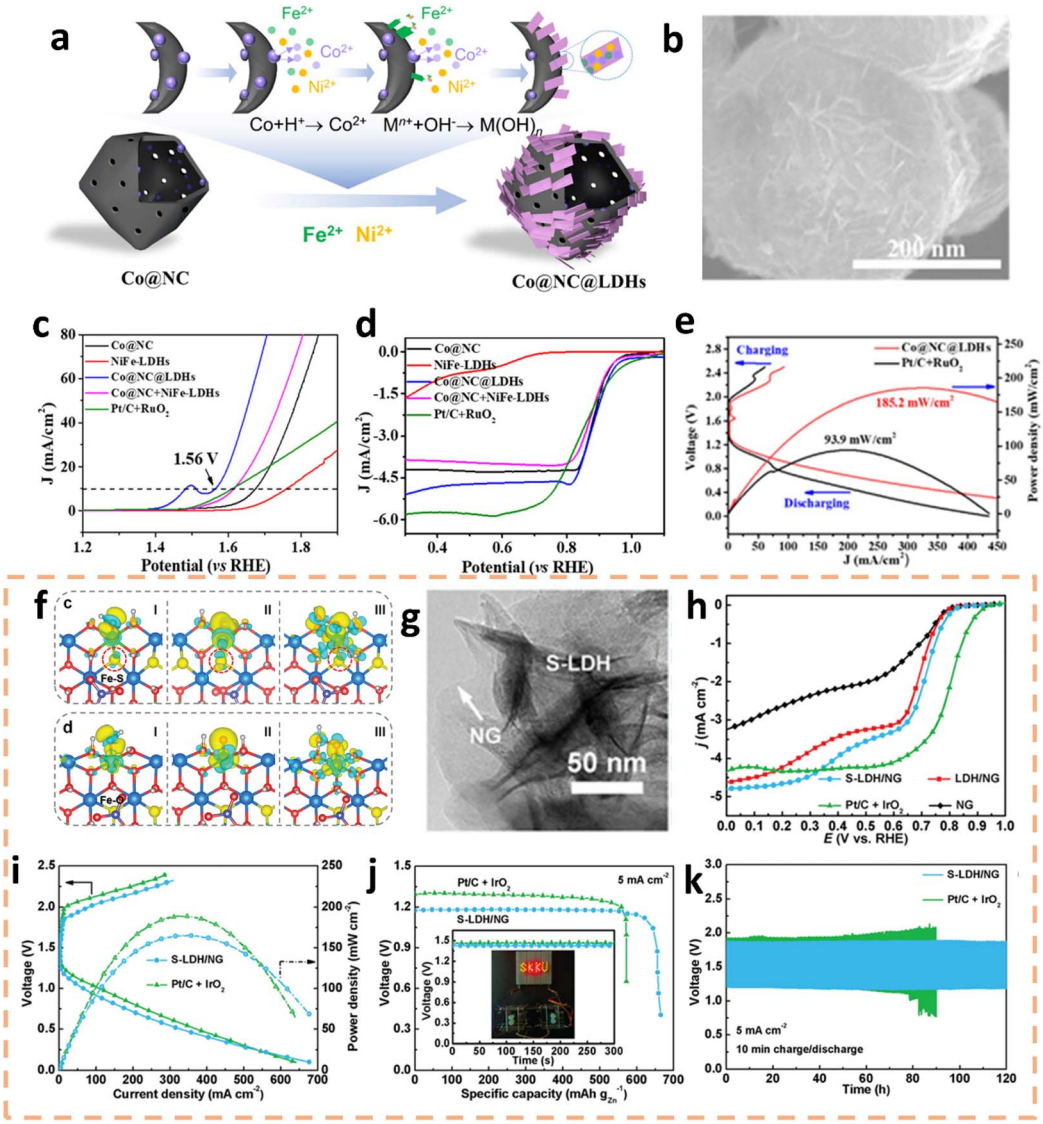

Fig. 13 (a) Schematic representation of the synthesis process for Co@NC@LDHs. (b) SEM images of Co@NC@LDHs. LSV curves for the OER (c) and ORR (d) of various catalysts including Co@NC, NiFe-LDHs, Co@NC@LDHs, Co@NC + NiFe-LDHs, and Pt/C + RuO_2. (e) Polarization and power density profiles for ZABs equipped with Co@NC@LDHs and Pt/C + RuO_2 catalysts. Reproduced with permission from ref. 182 Copyright 2023 Wiley-VCH. (f) Charge density difference mappings for intermediate species at the zigzag edge of the Fe–S and Fe–O sites. (g) TEM image of S-LDH. (h) ORR polarization curves of S-LDH/NG and other samples. Comparison of S-LDH/NG and Pt/C + IrO_2-based ZABs, showcasing charge/discharge polarization, power density (i), specific capacity (j), and cycling stability (k). Reproduced with permission from ref. 184 Copyright 2023, Wiley-VCH.

exceptional peak power density of 185.2 mW cm^{-2} and exhibited remarkable durability, sustaining over 500 hours of operation at a discharge current density of 5.0 mA cm^{-2} (Fig. 13e). The substitution of oxygen with sulfur in LDHs, due to their shared group in the periodic table, introduces new avenues for research.[183] Han *et al.* introduced lattice distortions and defect formations through sulfur-substituted LDHs, which were mismatched in size.[184] This manipulation of the electronic structure significantly enhanced the material's conductivity and catalytic activity (Fig. 13f). Experimental findings revealed that the onset potential of sulfur-substituted LDH on nitrogen-doped graphene (S-LDH/NG) in the ORR was 0.85 V. Notably, S-LDH/NG demonstrated outstanding performance in practical applications, achieving a peak power density of up to 165 mW cm^{-2} and an energy density of 772 W h kg_{Zn}^{-1} in ZABs, along with cycling stability for over 120 hours (Fig. 13h–k).

OER mechanisms are predicated on the adsorbate evolution mechanism (AEM), which hinges on the adsorption of intermediates at surface active sites. However, recent research has revealed that oxide catalysts can also function *via* the lattice oxygen mechanism (LOM), wherein lattice oxygen ions directly engage in the reaction. This mechanism enhances the migration capacity of oxygen ions by introducing oxygen vacancies or altering the lattice structure, thereby markedly elevating

catalytic activity.[185,186] Shao's team meticulously evaluated the OER performance across $LaSr_{2.00}$, $LaSr_{1.95}$, and $LaSr_{1.90}$ samples.[188] As the degree of strontium deficiency increased, there was a profound enhancement in the oxygen ion diffusion coefficient, with $LaSr_{1.90}$ attaining an exceptional value of 10^{-12} cm^2 s^{-1}, a substantial improvement over the 1.96×10^{-12} cm^2 s^{-1} observed for $LaSr_{2.00}$. This augmented diffusion rate is intricately linked to the enhanced OER activity, as evidenced by the requisite overpotential and current density parameters. Notably, to achieve 1 mA cm^{-2}, $LaSr_{1.90}$ exhibited a significantly reduced overpotential of 293 mV, in contrast to the 315 mV required for $LaSr_{2.00}$. Furthermore, at an applied potential of 1.60 V *versus* the reversible hydrogen electrode, $LaSr_{1.90}$ demonstrated a specific activity of 12.4 mA cm^{-2}, 2.6 times greater than that of $LaSr_{2.00}$. The lattice oxygen mechanism (LOM) thus emerges as a pivotal strategy for perovskite catalyst design and optimization, offering significant practical implications for ZABs.

This chapter not only elucidates the synthesis and performance evaluation of various catalytic materials but also delves into their practical applications within actual battery systems, discussing how to optimize battery performance by adjusting the electronic structure and configuration of catalytic sites. Critical endeavor will explore the electronic and chemical properties of these catalytic sites. Moreover, integrating these advanced catalytic materials to achieve more efficient and stable ZABs will be a significant direction for research in this field.

5. Key utilizations of nanostructured carbon electrodes in ZAB systems

5.1. Flexible ZABs

Over the years, the wearable electronics domain has increasingly acknowledged the potential of ZABs, attributed to their exceptional theoretical energy capacities, versatile designs, and adeptness at conforming to intricate geometries.[189–191] Despite considerable progress in the conception and assembly of pioneering flexible ZABs, the fabrication of electrodes that preserve optimal flexibility while ensuring robust performance in real-world applications continues to pose a significant challenge.[192,193] A fundamental challenge in developing flexible ZABs makes the air cathode malleable. Herein, porous carbon-centric cathodes with archetypes such as CNT paper, CNF textiles, graphene lamellae, and carbon aerogels, distinguished by their superior conductance, unwavering stability, and skilfully constructed porous structures, emerge as promising candidates for incorporation into flexible Zn–air matrices.[194–197]

Spray-coating represents a prevalent methodology for engineering flexible electrodes adorned with targeted electrocatalysts, contingent upon the availability of catalyst powders. The technique has been the focus of numerous seminal studies. Recently, Yu *et al.* reported the development of an FeN_4/G/FeCo catalyst *via* an advanced vapor-phase intercalation technique involving few-layer graphene and active sites, which demonstrated an impressively low overall overpotential of 0.648 V.[198] When this catalyst was meticulously spray-coated onto carbon cloth to fabricate a flexible zinc–air battery (FZAB) the device retained superior electrochemical performance despite undergoing repeated mechanical deformation (Fig. 14a). Notably, it achieved an open-circuit voltage of 1.46 V and, even under bending conditions, was capable of powering a light-emitting diode (LED) with an output of approximately 3 V. When configured in series, three cable-type ZABs are capable of generating over 4.0 V, which is adequately potent to recharge a smartphone (Fig. 14c). Furthermore, the battery exhibited exceptional charge–discharge cycling stability across various flexural states at 1 mA cm^{-2}, with a remarkable power density of 188 mW cm^{-2} and outstanding longevity (Fig. 14b), enduring over 450 cycles. The extraordinary performance can be ascribed to the synergistic interplay between the extensive surface area of the few-layer graphene and the atomic precision of the FeN_4 and FeCo alloy sites. This structural refinement effectively modulates the adsorption and desorption processes of the OOH* intermediate, thereby substantially enhancing the kinetics of both the ORR and the OER. In a parallel study, Tang *et al.* employed a sophisticated synthetic strategy to fabricate Co–N–C@mHCSs hybrid materials, demonstrating exceptional ORR activity in electrochemical performance evaluations.[201] The electrochemical workstation tests revealed that Co–N–C@mHCSs exhibited an $E_{1/2}$ of 0.81 V. Utilizing Co–N–C@mHCSs as the catalytic material, the electrodes were meticulously coated onto staggered electrode masks, followed by a drying process to form a uniform catalytic layer for cell assembly. The resulting battery exhibited an open-circuit voltage of 1.411 V and achieved a maximum power density of 178.4 mW cm^{-2}, underscoring its significant potential across multiple domains. Its versatility makes it particularly suitable for integration into wearable devices and portable electronics, as well as for use in biomedical sensors, especially in rapid diagnostics and health monitoring applications. Furthermore, the material's environmental stability and self-powering characteristics render it an ideal candidate for environmental monitoring and remote applications, supporting the broad deployment of smart cities and IoT devices. The malleability of oxygen electrodes fabricated through spray-coating predominantly depends on the ductility of the conductive base, with CNTs and graphene offering markedly better flexibility than carbon nanofiber (CNF) textiles. Moreover, establishing a durable bond between the electrocatalyst and the current collector poses a considerable challenge within spray-coating methodologies. The incorporation of conductive bases also adds to the aggregate mass of the apparatus. These elements are crucial in bolstering the batteries' cycling stability, discharge rate capabilities, and energy capacity. Consequently, devising an innovative synthesis technique that ensures sustained interaction and flexibility remains essential.

The *in situ* fabrication of freestanding electrocatalysts represents a highly advanced strategy designed to address the intrinsic limitations associated with conventional spray-coating methodologies. The synthesis of these freestanding electrocatalysts typically necessitates a meticulous design paradigm, often coupled with intricate post-synthesis processing techniques. As extensively documented in the existing corpus of

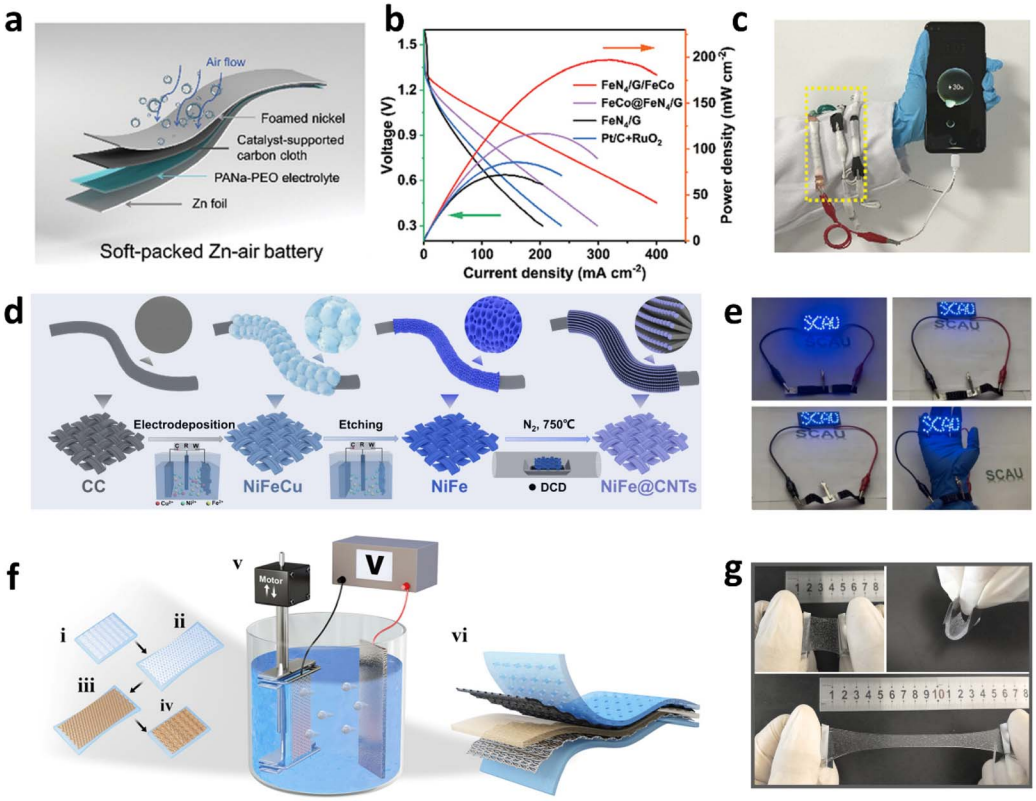

Fig. 14 (a) Flexible soft-packed ZAB configuration. (b) Performance curves of different catalysts in a ZAB. (c) Cable-type ZAB charging a mobile phone. Reproduced with permission from ref. 198 Copyright 2024, Elsevier. (d) Synthesis scheme for self-supported NiFe@CNTs. (e) Flexible ZABs prepared with NiFe@CNTs powering an LED screen. Reproduced with permission from ref. 199 Copyright 2024, Springer Nature. (f) Stages of fabricating a textile-based battery. (g) Flexibility demonstration of a CMC0.8%–PAA–KOH hydrogel membrane in various states.[200] Reproduced with permission from ref. 200 Copyright 2022 Wiley-VCH.

research, freestanding air cathodes, characterized by a high density of catalytically active sites and complex microarchitectures, can be fabricated through a diverse array of methodologies, including but not limited to hydrothermal synthesis, solvothermal processing, electrodeposition, and CVD. These methods may also be employed synergistically to optimize the properties of the resulting materials. The resultant composite freestanding air cathodes exhibit exceptional mechanical flexibility while maintaining robust catalytic performance under various deformation scenarios.

A quintessential example is the NiFe@CNTs catalyst, synthesized *in situ* on CC *via* CVD, which demonstrates outstanding catalytic proficiency for both the ORR and OER within the context of flexible, wearable ZABs (Fig. 14d).[199] This catalyst is distinguished by its 3D porous heterostructure, achieving a remarkably low overpotential of only 220 mV at 10 mA cm^{-2}, and a specific capacity reaching an impressive 936 W h kg_{Zn}^{-1}, thereby significantly surpassing the performance metrics of conventional Pt/C + RuO_2 catalysts. In solid-state ZABs, this material delivers 108 mW cm^{-2} peak power density and exceptional cycling stability, with performance retention exceeding 50% over an extended 425-hour operational period. The practical viability of FZABs for miniaturized or portable power supplies has been effectively demonstrated (Fig. 14e).

Moreover, the *in situ* growth of unsaturated CoN_3 on carbon nanotube-assembled necklace-like fibers (NLFs) has profoundly enhanced the electrocatalytic performance for both the ORR and the OER,[202] attributed to the intrinsic asymmetry of the CoN_3 sites. Electrochemical evaluations indicate that the CoN_3 NLF-based ZAB exhibits an exceptionally low overpotential of just 301 mV at 10 mA cm^{-2}, with an $E_{1/2}$ for the ORR reaching an outstanding 0.863 V, significantly surpassing the benchmarks set by conventional Pt/C and RuO_2-based catalysts. Furthermore, this ZAB delivers a remarkable discharge capacity of 687 mA h g_{Zn}^{-1} at a power density of 306 mW cm^{-2}, maintaining 88.7% of its current density over an extensive 300-hour high-rate cycling period. Importantly, the solid-state ZAB demonstrates remarkable operational stability and mechanical flexibility across a broad temperature spectrum, from −20 °C to 25 °C. At −20 °C, the power density exhibits a minimal decrease, with full performance restoration upon returning to 25 °C. Experimental findings underscore that the CoN_3 NLF-based ZAB can reliably power a light-emitting diode (LED) under various bending and torsional stresses, highlighting it's superior mechanical flexibility and robust environmental adaptability. The *in situ* growth of 3Dly ordered Co_3O_4@WO_3 composites on carbon cloth has exhibited a remarkable specific capacity of 828.6 mA h g_{Zn}^{-1} at 5 mA cm^{-2}, coupled with outstanding long-term stability,

maintaining nearly undiminished performance over an extensive 646-hour cycling test.[203] Crucially, the solid-state ZABs (ZABs) employing Co_3O_4@WO_3 as the cathode have demonstrated exceptional mechanical flexibility and operational stability at various bending angles of 0°, 60°, 90°, and 120°, highlighting their profound potential for flexible electronic applications. The incorporation of gel materials, featuring a distinct porous architecture, significantly enhances the permeability of both air and electrolyte, effectively mitigating the gas diffusion limitations characteristic of traditional compact fiber assemblies. The meticulously optimized interface design markedly elevates the catalytic efficiency, while the removal of polymer additives further augments electrical conductivity. Furthermore, the employment of directional freeze-casting technology allows for precise control over the material's microstructure, thereby amplifying its efficacy in battery applications. For example, a 3D porous honeycomb structure and N,S dual-doped carbon aerogel NSCA/FeCo, fabricated *via* this technique, achieves a peak power density of 132.0 mW cm^{-2} and a specific capacity of 804.5 W h kg^{-1}, while maintaining stable performance over more than 250 charge–discharge cycles.[204] Notably, the battery sustains excellent mechanical flexibility and operational stability even under diverse bending conditions, underscoring its robust performance and suitability for next-generation flexible energy storage devices.

Moreover, stretchability is a critical attribute of FABs, which can be achieved through the strategic design of stretchable electrodes and gel polymer electrolytes. Employing dynamic tensile electroplating, metallic-coated fabrics have been fabricated, wherein a CMC–PAA–KOH composite hydrogel serves as the electrolyte (Fig. 14f). These fabrics, endowed with a distinctive wavy architecture, maintain stable conductivity and high mechanical robustness even under 100% tensile strain (Fig. 14g). This innovative approach leverages the unique structural morphology to ensure that the metallic-coated fabric exhibits sustained electrical conductivity and mechanical integrity, thereby addressing the challenges associated with maintaining performance under significant deformation.[200]

This chapter delves deeply into the application of FZABs in wearable devices, noting that despite significant advancements, further enhancement of the batteries' practicality and flexibility is essential. Research should focus on developing ultra-flexible materials, optimizing electrode architectures, exploring highly extensible conductive substrates, and investigating integration methods for ZAB components. Particularly crucial is bolstering the ZAB's ability to recover performance after repeated physical deformations, a vital attribute for long-term wearable devices. Innovations in these key areas will better align future FZABs with the stringent demands of wearable technology, thereby advancing the development of smart wearable devices.

5.2. High-power ZABs

ZABs have emerged as compelling contenders in the energy storage field, owing to key metrics such as superior power density, excellent specific capacity, good cycle life, safety, and cost efficiency.[205] Despite their numerous advantages, they still face challenges, such as limited recharging cycles owing to dendrite formation on the Zn anode and subsequent short circuits. Nevertheless, the quantity of dendrite formation determines its resolution in the mechanical substitution of Zn fuel electrodes, allowing the battery to undergo rapid rejuvenation. Notably, this fuel replenishment process was remarkably efficient, culminating within five minutes, a temporal frame consistent with conventional daily refueling durations.

The preceding sections have thoroughly explored a range of carbon-based oxygen electrodes utilized in ZABs. Despite notable advancements in cathode catalyst engineering and the increasing interest due to their high specific energy, remarkable stability, and unique rechargeability, ZABs are hindered by the low conductivity of the gel electrolytes employed. Shang *et al.* innovatively developed a quasi-liquid gel electrolyte, demonstrating ionic conductivity on par with that of conventional liquid electrolytes.[206] By integrating macroscopic silica particles, they meticulously optimized the gel's porous structure (Fig. 15a and b), elevating its ionic conductivity to 562.6 mS cm^{-1} and reducing the alternating current (AC) impedance to 0.56 Ω. The p18@PAA gel exhibited exceptional specific capacity, achieving 787.05 mA h g_{Zn}^{-1} in discharge tests, supported by its superior electrolyte absorption and availability of OH^-, sustaining nearly 24 hours of continuous operation. These advancements significantly boosted the battery's peak power density to 154 mW cm^{-2} (Fig. 15c and d) and extended its operational cycle to over 40 hours, especially under minimal charge–discharge intervals. In rigorous charge/discharge tests at 10 mA cm^{-2}, the FZABs demonstrated commendable durability and rapidly recuperating performance even when subjected to mechanical deformation. The batteries consistently maintained voltage levels under various bending (Fig. 15e) conditions and successfully powered LEDs and an alarm clock.

Dendrite formation presents a critical challenge in the application of ZABs.[207,208] During the zinc deposition process, the emergence of irregular, dendritic crystalline structures can penetrate the battery separator, potentially causing short circuits and thereby compromising the battery's lifespan and safety. Furthermore, dendritic growth can impede electrolyte flow, adversely impacting the overall performance of the ZAB. Jiao *et al.* innovatively engineered a polarized polyacrylamide–sodium citrate (PAM–SC) gel electrolyte, characterized by a porous architecture with pore sizes ranging from 1 to 13 micrometers and enriched with polarized carboxylate (–COO–) groups.[209] These functional groups generate an intrinsic electric field between the gel electrolyte and the Zn anode, effectively mitigating the growth of zinc dendrites and stabilizing water molecules to reduce freeze–thaw cycles and evaporation. The PAM–SC gel demonstrates exceptional ionic conductivity, reaching 324.68 mS cm^{-1}, and exhibits a high water retention rate of 96.85%. The ZAB, employing a CoFe/AC catalyst, exhibits an $E_{1/2}$ comparable to that of 20% Pt/C in the ORR and matches the performance of RuO_2 at 1.69 V in the OER. The electrolyte surpasses traditional materials in discharge voltage and specific discharge capacity, achieving 744 mA h g^{-1}, with a power density of 107.64 mW cm^{-2}, thus demonstrating remarkable

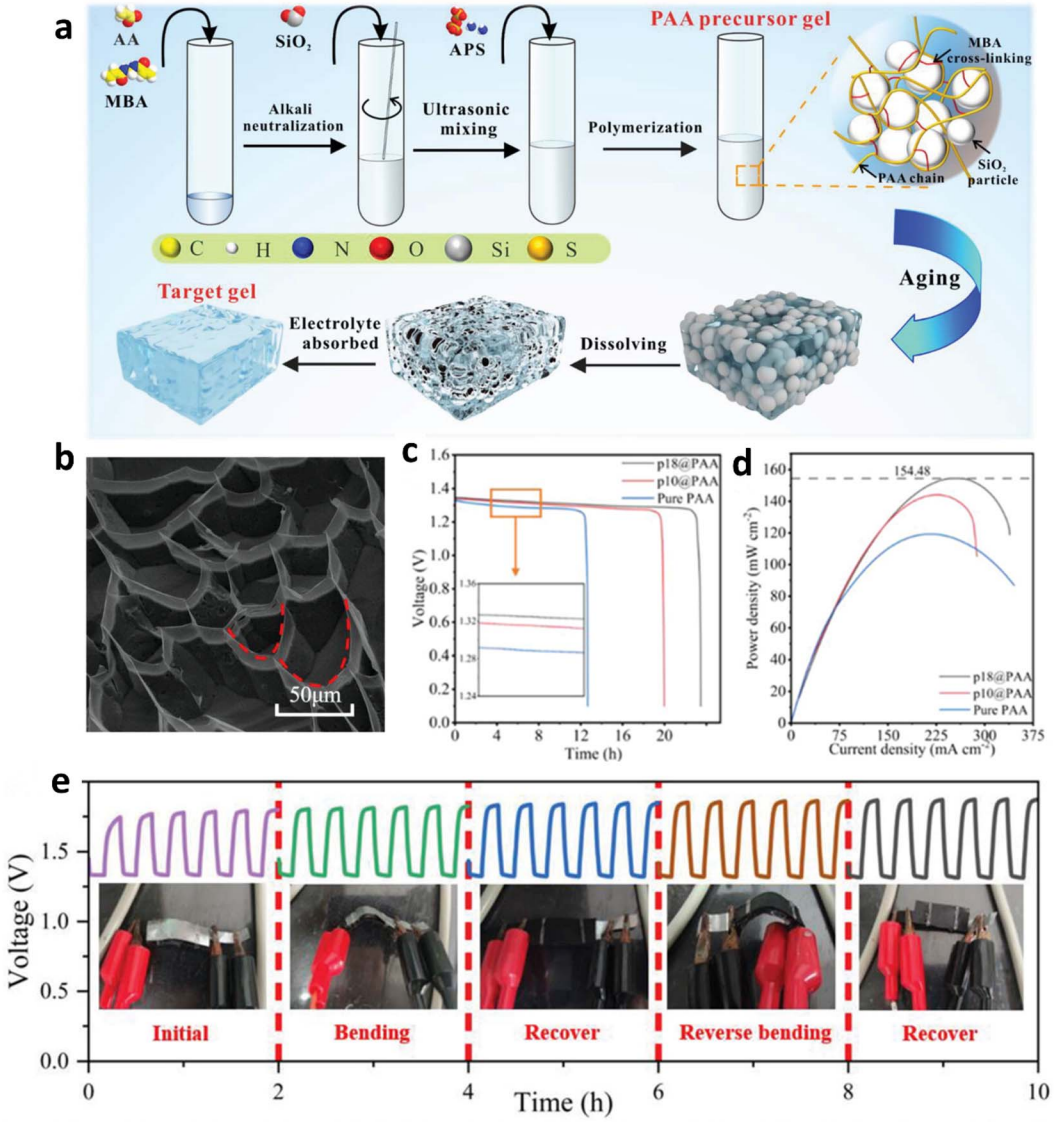

Fig. 15 (a) Mechanism of gel modification. (b) Cryo-SEM image of the cross-section of a pure PAA gel. (c) Discharge time of ZABs using p18@PAA gel. (d) Peak power density of ZABs with p18@PAA gel, surpassing that of other references. (e) Galvanostatic charge/discharge curves of a p18@PAA battery in different operating states. Reproduced with permission from ref. 206 Copyright 2023 Wiley-VCH.

efficiency and stability across a range of current densities. These FZABs can power devices such as fans or charging mobile phones when worn on the wrist and exhibit outstanding cycling durability over 700 cycles even under extreme conditions at −40 °C, highlighting their potential for applications in harsh operational environments.

Although ZABs exhibit significant theoretical energy density and cost-effectiveness, the formation of zinc dendrites and the low conductivity of electrolytes limit their broader application. To enhance battery performance and practicality, future research should focus on developing more efficient electrolyte formulations, exploring new materials that can inhibit the growth of zinc dendrites, optimizing electrode materials, and innovating system-level battery design integrations. These improvements will help advance the widespread application of ZABs in energy storage, particularly in markets prioritizing high energy efficiency and environmental sustainability.

6. Conclusions and perspectives

In conclusion, nanostructured porous carbon electrodes have witnessed considerable advancements in ZABs. By ingeniously designing the structure and catalytic sites, nanostructured porous carbon electrodes can significantly boost the efficacy of the ORR and the OER. However, most traditional reviews remain deficient in understanding the relationship between the structure and function. These gaps cover catalytic site design, nanoscale structures, and fabrication methods, causing porous catalysts to remain underexplored in comprehensive reviews. Therefore, this review focuses on the latest innovations in flexible and high-power ZABs, including reaction mechanisms,

structural properties, porous structure synthesis, and catalytic site adjustment. This review aims to assist readers in understanding the advantages, challenges, and prospective directions of porous catalysts. Despite these notable advancements, ongoing research still grapples with intricate challenges that will ultimately dictate the potential for ZABs to achieve broad commercial deployment.

(i) The relationship between the porous structure and electrochemical function is not fully delineated.[210] Mastery over pore size distribution, specific surface area, and pore channel configuration can amplify electroactivity. For example, extending surface area and porosity at the nanoscale could undermine mechanical integrity and endurance. Future research should focus on optimizing these features while exploring new synthesis and modification techniques. In particular, integrating advanced techniques with multiscale modeling could provide deeper insights into the internal reaction mechanisms of materials.

(ii) Porous carbon substrates play a significant role in ZABs. However, their susceptibility to corrosion at high oxidative potentials (OER process) often leads to the deactivation of ZABs. Several approaches have been employed to improve the corrosion resistance of carbon-based substrates, including graphitization enhancement, investigating alternative non-carbon substrates, applying protective coatings, creating corrosion-resistant materials, and reducing OER overpotential.

(iii) Choosing an appropriate electrolyte is critical for ZABs. Although traditional alkaline electrolytes exhibit high ionic conductivity, the zinc dendrite growth and carbonate formation issues have hindered the ZAB lifespan and safety. Future research directions should explore innovative electrolytes, such as ionic liquids or gel polymer electrolytes, to improve the cycling durability without sacrificing performance.

(iv) The widespread ZAB deployment faces numerous engineering challenges, especially for flexible devices that require ZABs to be mechanically adaptable while performing reliably under extreme conditions. Future research should integrate material optimization with innovative battery designs and advanced manufacturing methods, such as 3D printing techniques, to enhance the practicality of ZABs.

(v) Future research should emphasize interdisciplinary collaboration between fundamental science and applied technologies. By integrating insights from physical chemistry, computational science, and engineering technology, researchers can better understand and address the complex challenges facing ZABs. Furthermore, incorporating artificial intelligence and machine learning can enhance data-driven material design and performance prediction, accelerating the discovery and development of new high-performance electrode and electrolyte materials.

In conclusion, although ZABs have demonstrated immense potential, achieving their widespread application in energy storage still requires extensive exploration in material design, electrolyte optimization, and integration of systems. Through continuous innovation, ZABs are poised to become a significant component of efficient and sustainable energy storage technologies.

Data availability

No primary research results, software or code have been included and no new data were generated or analysed as part of this review.

Author contributions

Sanshuang Gao and Maolin Li: writing and original draft preparation, data curation, conceptualization. Nianpeng Li and Qian Liu: validation, project administration, data curation. Lei Zhang and Xinzhong Wang: writing – review & editing, supervision, project administration, conceptualization, funding acquisition. Guangzhi Hu: writing – review and editing, supervision, funding acquisition.

Conflicts of interest

There are no conflicts to declare.

Acknowledgements

This work was supported by the National Natural Science Foundation of China-Yunnan Joint Fund (U2002213), the Qilu Lake Field Observation and Research Station for Plateau Shallow Lake in Yunnan Province (202305AM070001), the Tianshan Innovation Team Plan of Xinjiang Uygur Autonomous Region (2023D14002), the Open Foundation of Guangxi Key Laboratory of Processing for Non-Ferrous Metals and Featured Materials (2022GXYSOF10), and the Double First University Plan (C176220100042).

References

1 L. Xiao, W. Ren, S. Shen, M. Chen, R. Liao, Y. Zhou and X. Li, *Acta Phys.-Chim. Sin.*, 2023, **40**, 2308036.
2 Z. Niu, Y. Gao, T. Wu, F. Zhang, R. Zhao, Z. Chen, Y. Yuan, T. Jiao, J. Gu, L. Lu and D. Wang, *Carbon Energy*, 2024, **6**, 535.
3 Y. Liu, L. Li, L. Wang, N. Li, X. Zhao, Y. Chen, T. Sakthivel and Z. Dai, *Nat. Commun.*, 2024, **15**, 2851.
4 Y. Jiang, Y. Wang, G. Cheng, Y. Li, L. Dai, J. Zhu, W. Meng, J. Xi, L. Wang and Z. He, *Carbon Energy*, 2024, **6**, 537.
5 Y. Tong, X. Huang, N. Liu, R. Zhao and G. Hu, *Desalination*, 2024, **586**, 117852.
6 Z. Nie, M. Chen, L. Zhang, Q. Feng, J. Hu, X. Huang, C. Zhou, Y. Zhou, T. Wågberg and G. Hu, *Chem. Eng. J.*, 2023, **463**, 142411.
7 X. Sun, Y. Zhou, D. Li, K. Zhao, L. Wang, P. Tan, H. Dong, Y. Wang and J. Liang, *Carbon Energy*, 2024, **6**, e539.
8 J. Wang, X. Chen, J. Wang, X. Cui, Z. Wang, G. Zhang, W. Lyu, M. Shkunov, S. R. P. Silva, Y. Liao, K. Yang and W. Yan, *Carbon Energy*, 2024, e572, DOI: **10.1002/cey2.572**.
9 Y. Gao, H. Zhang, J. Peng, L. Li, Y. Xiao, L. Li, Y. Liu, Y. Qiao and S. L. Chou, *Carbon Energy*, 2024, **6**, e464.
10 H. Shi, S. Gao, X. Liu, Y. Wang, S. Zhou, Q. Liu, L. Zhang and G. Hu, *Small*, 2024, **20**, e2309557.

11 Q. Xu, J. Hu, H. Yao, J. Lei, C. Zhou, L. Zhang and H. Pang, *ACS Appl. Mater. Interfaces*, 2024, **16**, 42352–42362.
12 J. Hu, Q. Xu, X. Wang, X. Huang, C. Zhou, Y. Ye, L. Zhang and H. Pang, *Carbon Energy*, 2023, **5**, 315.
13 H. Gong, G. Sun, W. Shi, D. Li, X. Zheng, H. Shi, X. Liang, R. Yang and C. Yuan, *Carbon Energy*, 2024, **6**, 432.
14 X. Liu, S. Chen, H. Wang, A. Liu, S. Wen, L. Mi and Y. Li, *Nano Res.*, 2023, **16**, 6701–6709.
15 X. Cai, L. Lai, J. Lin and Z. Shen, *Mater. Horiz.*, 2017, **4**, 945–976.
16 H.-F. Wang, C. Tang and Q. Zhang, *Adv. Funct. Mater.*, 2018, **28**, 1803329.
17 H. Liu, W. Xie, Z. Huang, C. Yao, Y. Han and W. Huang, *Small Methods*, 2022, **6**, 2101116.
18 Z. Nie, L. Zhang, Z. Du, J. Hu, X. Huang, C. Zhou, T. Wagberg and G. Hu, *J. Colloid Interface Sci.*, 2023, **642**, 714–723.
19 Y.-T. Zhang, F. Zhang, Z. Lu, J.-M. Luo, S.-Y. Feng, Q. Wang, H. Chen, H.-M. Wu, Z.-P. Miao, B. Chi, N. Yu, C.-H. You, J. Li and X.-L. Tian, *Rare Met.*, 2024, **43**, 4973–4981.
20 L. Li, N. Li, J.-W. Xia, S.-L. Zhou, X.-Y. Qian, F.-X. Yin, G.-H. Dai, G.-Y. He and H.-Q. Chen, *Nano Res.*, 2023, **16**, 9416–9425.
21 Y. Ye, L. Zhang, Z. Nie, N. Li, S. Zhou, H. Wang, T. Wågberg and G. Hu, *Chem. Eng. J.*, 2022, **446**, 137210.
22 Y. Zhang, Y. Jiang, A. Abdukayum, X. Xie, S. Gao, X. Liu, L. Zhang, Q. Liu and G. Hu, *Mater. Today Energy*, 2024, **44**, 101641.
23 D. Wang, H. Xu, P. Yang, L. Xiao, L. Du, X. Lu, R. Li, J. Zhang and M. An, *J. Mater. Chem. A*, 2021, **9**, 9761–9770.
24 H. Zuo, Z. Zhao, Y. He, S. Li, X. Li, Z. Cheng, C. Cheng, A. Thomas and Y. Liao, *Carbon*, 2023, **201**, 984–990.
25 M. Shen, J. Liu, J. Li, C. Duan, C. Xiong, W. Zhao, L. Dai, Q. Wang, H. Yang and Y. Ni, *Energy Storage Mater.*, 2023, **59**, 102790.
26 J. W. Liang, J. P. Chen, G. L. Wang, J. J. Liu, N. G. Wang and Z. C. Shi, *ACS Appl. Mater. Interfaces*, 2022, **14**, 48789–48800.
27 Q. Xu, L. Zhang, H. Zhao, X. Yin, A. Wang, X. Li and G. Hu, *Colloids Surf., A*, 2024, **701**, 134986.
28 D. Guo, Y. Fu, F. Bu, H. Liang, L. Duan, Z. Zhao, C. Wang, A. M. El-Toni, W. Li and D. Zhao, *Small Methods*, 2021, **5**, e2001137.
29 X. Yang, H. Mao, Z. Zhou, K. Li, C. Li, Q. Ye, B. Liu, Y. Fang and X. Cai, *Adv. Funct. Mater.*, 2024, **34**, 2402933.
30 Y. Peng, F. Zhang, Y. Zhang, X. Luo, L. Chen and Y. Shi, *J. Colloid Interface Sci.*, 2022, **616**, 659–667.
31 J. Ma, J. Li, R. Wang, Y. Yang, P. Yin, J. Mao, T. Ling and S. Qiao, *Mater. Today Energy*, 2021, **19**, 100624.
32 J. Y. Zhang, C. Xia, Y. Su, L. Zu, Z. Zhao, P. Li, Z. Lv, J. Wang, B. Mei, K. Lan, T. Zhao, P. Zhang, W. Chen, S. Zaman, Y. Liu, L. Peng, B. Y. Xia, A. Elzatahry, W. Li and D. Zhao, *Small*, 2024, **20**, 2307378.
33 F. Wang, K. Qiu, Z. Zhang, X. Li, Y. Cao and F. Wang, *Small*, 2023, **19**, e2303151.
34 S. Ji, Y. Wang, H. Liu, X. Lu, C. Guo, S. Xin, J. H. Horton, F. Zhan, Y. Wang and Z. Li, *Adv. Funct. Mater.*, 2024, **34**, 2314621.
35 H. Wang, Y. Jiao, S. Wang, P. Ye, J. Ning, Y. Zhong and Y. Hu, *Small*, 2021, **17**, 2103517.
36 Y. Hao, Y. Kang, Y. Mi, W. Wang and Z. Lei, *J. Colloid Interface Sci.*, 2021, **598**, 83–92.
37 S. J. Kim, J. H. Hong, J.-K. Lee and Y. C. Kang, *J. Mater. Chem. A*, 2021, **9**, 25160–25167.
38 J. Hong, L. Zhang, Q. Zhu, Z. Du, Y. Zhou, T. Wagberg and G. Hu, *Mater. Horiz.*, 2023, **10**, 5969–5982.
39 Z. Meng, N. Chen, S. Cai, J. Wu, R. Wang, T. Tian and H. Tang, *Nano Res.*, 2021, **14**, 4768–4775.
40 F. Zhang, X. Liu, Y. Chen, M. Tian, T. Yang, J. Zhang and S. Gao, *Chin. Chem. Lett.*, 2023, **34**, 108142.
41 Y. Zhou, Y. Liu, Y. Yan, Z. Yi, Y. Li and C.-M. Chen, *Chin. Chem. Lett.*, 2024, 109569.
42 K. Ding, J. Hu, J. Luo, L. Zhao, W. Jin, Y. Liu, Z. Wu, G. Zou, H. Hou and X. Ji, *Adv. Funct. Mater.*, 2022, **32**, 2207331.
43 Y. Liu, S. Liu, P. Zhang, J. Zhou, H. Liu, S. Li, X. Li, X. Wang, D. Han, Y. Chen, Y. Wang, J. Jiang and B. Li, *Adv. Funct. Mater.*, 2024, **34**, 2400522.
44 X. Xie, H. Peng, K. Sun, W. Li, A. Liang, G. Ma, Z. Lei and Y. Xu, *Adv. Funct. Mater.*, 2024, **34**, 2316037.
45 C. Chen, J. Chai, M. Sun, T. Guo, J. Lin, Y. Zhou, Z. Sun, F. Zhang, L. Zhang, W. Chen and Y. Li, *Energy Environ. Sci.*, 2024, **17**, 2298–2308.
46 R. Luo, R. Wang, Z. Meng, Y. Xia and H. Tang, *Adv. Compos. Hybrid Mater.*, 2023, **6**, 105.
47 K. Ding, Y. Ye, J. Hu, L. Zhao, W. Jin, J. Luo, S. Cai, B. Weng, G. Zou, H. Hou and X. Ji, *Nano-Micro Lett.*, 2023, **15**, 28.
48 M. G. Park, J. Hwang, Y. P. Deng, D. U. Lee, J. Fu, Y. Hu, M. J. Jang, S. M. Choi, R. Feng, G. Jiang, L. Qian, Q. Ma, L. Yang, Y. S. Jun, M. H. Seo, Z. Bai and Z. Chen, *Adv. Mater.*, 2024, **36**, e2311105.
49 J. Zhang, X. Dong, G. Wang, J. Chen and R. Wang, *Appl. Catal., B*, 2024, **342**, 123459.
50 L. Yan, B. Xie, C. Yang, Y. Wang, J. Ning, Y. Zhong and Y. Hu, *Adv. Energy Mater.*, 2023, **13**, 2204245.
51 Y. Wei, H. Xia, H. Lan, D. Xue, B. Zhao, Y. Yu, Y. Hu and J. N. Zhang, *Adv. Energy Mater.*, 2023, **14**, 2303011.
52 P. Li, F. Qiang, X. Tan, Z. Li, J. Shi, S. Liu, M. Huang, J. Chen, W. Tian, J. Wu, W. Hu and H. Wang, *Appl. Catal., B*, 2024, **340**, 123231.
53 J. Li, Y. Kang, Z. Lei and P. Liu, *Appl. Catal., B*, 2023, **321**, 122029.
54 J. Zhang, F. Tang, K. Wan, Y. Yang, C. Zhang, P. W. Ming and B. Li, *J. Mater. Chem. A*, 2022, **10**, 14866–14874.
55 Y. Tan, W. Zhu, Z. Zhang, W. Wu, R. Chen, S. Mu, H. Lv and N. Cheng, *Nano Energy*, 2021, **83**, 105813.
56 X. Xie, L. Peng, H. Yang, G. I. N. Waterhouse, L. Shang and T. Zhang, *Adv. Mater.*, 2021, **33**, 2101038.
57 Z.-D. Wang, S. Liang, C.-K. Bai, Z.-F. Guo, G.-L. Lu, H. Sun, Z.-N. Liu and H.-Y. Zang, *J. Mater. Chem. A*, 2022, **10**, 3169–3177.
58 Z. Liang, N. Kong, C. Yang, W. Zhang, H. Zheng, H. Lin and R. Cao, *Angew. Chem., Int. Ed.*, 2021, **60**, 12759–12764.
59 J. Hong, M. Chen, L. Zhang, L. Qin, J. Hu, X. Huang, C. Zhou, Y. Zhou, T. Wågberg and G. Hu, *Chem. Eng. J.*, 2023, **455**, 140401.

60 Z. Li, L. Zhang, Q. Zhu, Z. Ke and G. Hu, *J. Colloid Interface Sci.*, 2024, **653**, 1577–1587.
61 X. Li, L. Fan, B. Xu, Y. Shang, M. Li, L. Zhang, S. Liu, Z. Kang, Z. Liu, X. Lu and D. Sun, *ACS Appl. Mater. Interfaces*, 2021, **13**, 53892–53903.
62 Y. Zeng, Z. Pei, D. Luan and X. W. D. Lou, *J. Am. Chem. Soc.*, 2023, **145**, 12333–12341.
63 Z. Nie, L. Zhang, Q. Zhu, Z. Ke, Y. Zhou, T. Wågberg and G. Hu, *J. Energy Chem.*, 2024, **88**, 202–212.
64 Z. Liu, Y. Zhu, K. Xiao, Y. Xu, Y. Peng, J. Liu and X. Chen, *ACS Appl. Mater. Interfaces*, 2021, **13**, 24710–24722.
65 X. Guo, S. Liu, X. Wan, J. Zhang, Y. Liu, X. Zheng, Q. Kong and Z. Jin, *Nano Lett.*, 2022, **22**, 4879–4887.
66 L. Wu, R. Zhao, G. Du, H. Wang, M. Hou, W. Zhang, P. Sun and T. Chen, *Green Energy Environ.*, 2023, **8**, 1693–1702.
67 J. Long, C. Chen and X. Gou, *J. Colloid Interface Sci.*, 2022, **625**, 555–564.
68 Y. Zhang, Y. Li, K. Shi, Z. Zhu, X. Li, H. Xu and J. Gao, *J. Alloys Compd.*, 2022, **925**, 166680.
69 X. Lu, H. Xu, P. Yang, L. Xiao, Y. Li, J. Ma, R. Li, L. Liu, A. Liu, V. Kondratiev, O. Levin, J. Zhang and M. An, *Appl. Catal., B*, 2022, **313**, 121454.
70 W. Xiao, D. Yan, Q. Zhao, D. Bukhvalov and X. Yang, *Appl. Catal., B*, 2024, **346**, 123740.
71 M. Xu, L. Zhang, X. Liang, H. Xiao, H. Zhuang, F. Zhang, T. Zhang, P. Han, W. Dai, F. Gao, J. Zhang, L. Zheng and Q. Gao, *Appl. Catal., B*, 2024, **349**, 123866.
72 C. Li, Y. Zhang, M. Yuan, Y. Liu, H. Lan, Z. Li, K. Liu and L. Wang, *Chem. Eng. J.*, 2023, **471**, 144515.
73 L. Yang, X. Yao, C. Du, Z. Han, M. Jin, S. Peng, X. Ma, Y. Zhu, M. Zou and C. Cao, *Chem. Eng. J.*, 2024, **481**, 148598.
74 J. Ran, M. Si and D. Gao, *Chem. Eng. J.*, 2024, **493**, 152545.
75 C. Xu, L. Chen, H. Zhou, S. Qin, Z. Hou, Y. Chen, J. Sun, J. Xu and Z. Huang, *J. Energy Chem.*, 2024, **97**, 612–621.
76 A. De, M. S. Kim, A. Adhikari, R. Patel and S. Kundu, *J. Mater. Chem. A*, 2024, **12**, 19720–19756.
77 J. X. Flores-Lasluisa, M. García-Rodríguez, D. Cazorla-Amorós and E. Morallón, *Carbon*, 2024, **225**, 119147.
78 Y. Dai, J. Yu, P. Tan, C. Cheng, T. Liu, S. Zhao, Z. Shao, T. Zhao and M. Ni, *J. Power Sources*, 2022, **525**, 231108.
79 S. Zhu, T. Wu, M. Liao, J. Meng, Y. Xie and C. Lu, *Chem. Eng. J.*, 2024, **484**, 149693.
80 L. Cui, K. Fan, L. Zong, F. Lu, M. Zhou, B. Li, L. Zhang, L. Feng, X. Li, Y. Chen and L. Wang, *Energy Storage Mater.*, 2022, **44**, 469–476.
81 L. Zong, F. Lu, W. Zhang, K. Fan, X. Chen, B. Johannessen, D. Qi, N. M. Bedford, M. Warren, C. U. Segre, P. Liu, L. Wang and H. Zhao, *Energy Storage Mater.*, 2022, **49**, 209–218.
82 M. Li, Y. Wang, Y. Zheng, G. Fu, D. Sun, Y. Li, Y. Tang and T. Ma, *Adv. Energy Mater.*, 2020, **10**, 1903833.
83 M. Ding, X. Hui and L. Yin, *Electrochim. Acta*, 2023, **468**, 142891.
84 M. Wei, K. Wang, P. Pei, Y. Zuo, L. Zhong, N. Shang, H. Wang, J. Chen, P. Zhang and Z. Chen, *Appl. Energy*, 2022, **324**, 119690.
85 S. Wu, H. Zhao, X. Xu, C. Liu, P. Zhang, S. Fu, Q. Su, Y. Sun, Q. Yang and H. Peng, *J. Alloys Compd.*, 2022, **926**, 166777.
86 Y. Cha, T. Kim, K. Kim, J. W. Seo, H. Y. Jang and W. Choi, *Carbon*, 2024, **220**, 118859.
87 L. Zhang, H. Jiang, M. Tang, Y. Jiang, B. Tang, H. Tan, Y. Kong and H. Hu, *Appl. Catal., B*, 2024, **354**, 124151.
88 L. Li, L. Zhang, Z. Nie, W. Ma, N. Li, T. Wågberg and G. Hu, *J. Mater. Chem. A*, 2022, **10**, 21659–21671.
89 Z. Qi, Z. Lu, X. Guo, J. Jiang, S. Liu, J. Sun, X. Wang, J. Zhu and Y. Fu, *Small*, 2024, **20**, e2401221.
90 Z. H. Bi, H. Zhang, X. Zhao, Y. W. Wang, F. Tan, S. Q. Chen, L. G. Feng, Y. T. Zhou, X. Ma, Z. Su, X. Z. Wang, T. Wågberg and G. Z. Hu, *Energy Storage Mater.*, 2023, **54**, 313–322.
91 Y. Wu, C. Ye, L. Yu, Y. Liu, J. Huang, J. Bi, L. Xue, J. Sun, J. Yang, W. Zhang, X. Wang, P. Xiong and J. Zhu, *Energy Storage Mater.*, 2022, **45**, 805–813.
92 X. F. Gong, J. B. Zhu, J. Z. Li, R. Gao, Q. Y. Zhou, Z. Zhang, H. Z. Dou, L. Zhao, X. L. Sui, J. J. Cai, Y. L. Zhang, B. Liu, Y. F. Hu, A. P. Yu, S. H. Sun, Z. B. Wang and Z. W. Chen, *Adv. Funct. Mater.*, 2021, **31**, 2008085.
93 Y. Liu, Z. Chen, N. Zhao, G. Tong, Z. Li, B. Wang, Y. Du, Q. Pan, Z. Li, Y. Xie and Y. Yang, *Chem. Eng. J.*, 2022, **433**, 134469.
94 H. Chang, X. Liu, S. Zhao, Z. Liu, R. Lv, Q. Zhang and T. F. Yi, *Adv. Funct. Mater.*, 2023, **34**, 2313491.
95 T. Han, H. Sun, J. Hu, N. Sun, Y. Liu, J. Chen, M. Chen and D. Cao, *Carbon*, 2024, **223**, 119025.
96 N. K. Wagh, S. S. Shinde, C. H. Lee, S. H. Kim, D. H. Kim, H. D. Um, S. U. Lee and J. H. Lee, *Nano-Micro Lett.*, 2022, **14**, 190.
97 X. Shu, Q. Chen, M. Yang, M. Liu, J. Ma and J. Zhang, *Adv. Energy Mater.*, 2022, **13**, 2202871.
98 X. Wang, Y. Yang, R. Wang, L. Li, X. Zhao and W. Zhang, *Langmuir*, 2022, **38**, 7280–7289.
99 F. Zhang, X. Liu, Y. Chen, M. Tian, T. Yang, J. Zhang and S. Gao, *Chin. Chem. Lett.*, 2023, **34**, 108142.
100 J. Dou, M. Qi, H. Wang, W. Shi, X. Luan, W. Guo, L. Xiao, C. Zhao, D. Cheng, T. Jiang, W. Zhang, W. Bian and B. Zhou, *Microporous Mesoporous Mater.*, 2021, **320**, 111101.
101 L. Qiu, Q. Wang, P. Yan and X. Yu, *J. Mater. Chem. A*, 2022, **10**, 21251–21259.
102 P. Wei, X. G. Li, Z. M. He, X. P. Sun, Q. R. Liang, Z. Y. Wang, C. Fang, Q. Li, H. Yang, J. T. Han and Y. H. Huang, *Chem. Eng. J.*, 2021, **422**, 130134.
103 C. Hu, Q. R. Liang, Y. T. Yang, Q. M. Peng, Z. Y. Luo, J. X. Dong, T. T. Isimjan and X. L. Yang, *J. Colloid Interface Sci.*, 2023, **633**, 500–510.
104 G. Y. Ye, S. Q. Liu, K. M. Zhao and Z. He, *Angew. Chem., Int. Ed.*, 2023, **62**, e202303409.
105 Y. L. Xia, Z. Z. Zhang, F. X. Qin, J. Gao, H. Wang, Z. W. Xu, X. Y. Tan, X. Liu, X. F. Li and Z. Yin, *J. Appl. Electrochem.*, 2021, **51**, 669–679.
106 M. X. Zhang, H. Peng, K. J. Sun, X. Xie, X. F. Lei, S. T. Liu, G. F. Ma and Z. Q. Lei, *Chin. J. Chem.*, 2022, **40**, 2763–2772.
107 T. T. Lu, X. L. Hu, J. J. He, R. Li, J. Gao, Q. Lv, Z. Yang, S. Cui and C. S. Huang, *Nano Energy*, 2021, **85**, 106024.

108 P. Liu, Y. Liu, K. Wang, S. Shi, M. Jin, J. Liu, T. Qin, Q. Liu, X. Liu and J. He, *Nano Res.*, 2024, **17**, 7957–7966.
109 K. Gong, F. Du, Z. Xia, M. Durstock and L. Dai, *Science*, 2009, **323**, 760–764.
110 T. Thiruppathiraja, A. L. Arokiyanathan and S. Lakshmipathi, *Fuel Cells*, 2021, **21**, 490–501.
111 Q. Guo, S. Ma, Q. L. Wu, Z. Z. Liu, Z. Q. Yao, S. Li, J. P. Zhao and F. C. Liu, *Inorg. Chem. Front.*, 2023, **10**, 3867–3873.
112 Z. Z. Duan, G. K. Han, H. Huo, Z. Y. Lin, L. P. Ge, C. Y. Du, Y. Z. Gao and G. P. Yin, *ACS Sustainable Chem. Eng.*, 2021, **9**, 1264–1271.
113 R. Takada, Y. Shu, Y. Taniguchi, X. R. Yang, K. Miyake, Y. Uchida and N. Nishiyama, *Carbon*, 2024, **218**, 118719.
114 W. Ding, A. Saad, Y. Wu, Z. Wang and X. Li, *Nano Res.*, 2023, **16**, 4793–4802.
115 W. K. Wang, W. Zhang, Y. J. Cai, Q. Wang, J. Deng, J. S. Chen, Z. F. Jiang, Y. Z. Zhang and C. Yu, *Nano Res.*, 2023, **16**, 2177–2184.
116 J. M. Liu, C. B. Wang, Y. P. Song, S. Zhang, Z. H. Zhang, L. H. He and M. Du, *J. Colloid Interface Sci.*, 2021, **591**, 253–263.
117 Y. Arafat, M. R. Azhar, Y. J. Zhong, M. O. Tadé and Z. P. Shao, *Mater. Res. Bull.*, 2021, **140**, 111315.
118 S. Y. Zhang, W. G. Yang, Y. L. Liang, X. Yang, M. N. Cao and R. Cao, *Appl. Catal., B*, 2021, **285**, 119780.
119 X. B. Ding, F. Li, Q. C. Cao, H. Wu, Y. H. Qin, Y. Li, T. L. Wang, X. T. Zheng and C. W. Wang, *Chem. Eng. J.*, 2022, **429**, 132469.
120 X. J. Zheng, J. Wu, X. C. Cao, J. Abbott, C. Jin, H. B. Wang, P. Strasser, R. Z. Yang, X. Chen and G. Wu, *Appl. Catal., B*, 2019, **241**, 442–451.
121 S. Halder, A. K. Pradhan, P. Sivasakthi, P. K. Samanta and C. Chakraborty, *Mater. Today Chem.*, 2023, **32**, 101649.
122 H. Lei, M. W. Cui and Y. Huang, *ACS Appl. Mater. Interfaces*, 2022, **14**, 34793–34801.
123 W. Li, J. Y. Wang, C. G. Jia, J. X. Chen, Z. H. Wen and A. S. Huang, *J. Colloid Interface Sci.*, 2023, **650**, 275–283.
124 R. Su, X. Tao, K. Zheng, L. Jiao, C. Zhang, R. Yang, H. Xie, X. Meng and C. Xu, *Carbon*, 2024, **225**, 119125.
125 C. Jin, H. Deng, J. Zhang, Y. Hao and J. Liu, *Chem. Eng. J.*, 2022, **434**, 134617.
126 X. Feng, G. Chen, Z. Cui, R. Qin, W. Jiao, Z. Huang, Z. Shang, C. Ma, X. Zheng, Y. Han and W. Huang, *Angew. Chem., Int. Ed.*, 2024, **63**, e202316314.
127 T. Li, Y. Liu, Y. Huang, L. Zhang, Z. Chen, W. Yang, G. Shi, J. Zhou, R. Zou, J. Gan, L. Zhong and X. Peng, *Small*, 2024, **20**, e2311675.
128 J. C. Li, Y. Meng, L. Zhang, G. Li, Z. Shi, P. X. Hou, C. Liu, H. M. Cheng and M. Shao, *Adv. Funct. Mater.*, 2021, **31**, 2103360.
129 Y. Meng, J.-C. Li, S.-Y. Zhao, C. Shi, X.-Q. Li, L. Zhang, P.-X. Hou, C. Liu and H.-M. Cheng, *Appl. Catal., B*, 2021, **294**, 120239.
130 M. Yi, N. Li, B. Lu, L. Li, Z. Zhu and J. Zhang, *Energy Storage Mater.*, 2021, **42**, 418–429.
131 T. Zhou, Y. Guan, C. He, L. Zhang, X. Sun, Z. Song, Q. Zhang, C. He, X. Jiang, Z. Luo, W. Xing and X. Ren, *Carbon Energy*, 2024, **6**, e477.
132 C. L. Jiao, Z. Xu, J. Z. Shao, Y. Xia, J. Tseng, G. Y. Ren, N. J. Zhang, P. F. Liu, C. X. Liu, G. S. Li, S. Chen, S. Q. Chen and H. L. Wang, *Adv. Funct. Mater.*, 2023, **33**, 2213897.
133 Z. Wang, X. Jin, R. Xu, Z. Yang, S. Ma, T. Yan, C. Zhu, J. Fang, Y. Liu, S. J. Hwang, Z. Pan and H. J. Fan, *ACS Nano*, 2023, **17**, 8622–8633.
134 M. X. Shen, J. Liu, J. Li, C. Duan, C. Y. Xiong, W. Zhao, L. Dai, Q. Y. Wang, H. Yang and Y. H. Ni, *Energy Storage Mater.*, 2023, **59**, 102790.
135 D. L. Cao, Y. W. Mu, L. J. Liu, Z. X. Mou, S. Chen, W. J. Yan, H. Q. Zhou, T. S. Chan, L. Y. Chang, L. Song, H. J. Zhai and X. J. Fan, *ACS Nano*, 2024, **18**, 11474–11486.
136 J.-C. Li, Y. Meng, H. Zhong, L. Zhang, S. Ding, Z. Lyu, S. P. Beckman, P.-X. Hou, Y. Mei, H.-M. Cheng and C. Liu, *Carbon*, 2023, **205**, 302–309.
137 Y. Zhang, L. Chen, B. Yan, F. Zhang, Y. Shi and X. Guo, *Composites, Part B*, 2023, **253**, 110575.
138 T. Yu, X. T. Cao, R. L. Song, L. Li, X. Dong, J. N. Li, X. Wang, X. S. Zhou, N. Y. Yuan and J. N. Ding, *J. Alloys Compd.*, 2023, **939**, 168679.
139 J. Li, Y. Kang, W. Wei, X. Li, Z. Lei and P. Liu, *Chem. Eng. J.*, 2021, **407**, 127961.
140 Z. Huang, Y. Wang, Y. Xiao, X. Zhou, M. Zhang and P. Yu, *ACS Sustainable Chem. Eng.*, 2024, **12**, 9727–9736.
141 X. Xie, H. Peng, K. Sun, X. Lei, R. Zhu, Z. Zhang, G. Ma and Z. Lei, *Chem. Eng. J.*, 2023, **452**, 139253.
142 H. Lei, L. Ma, Q. X. Wan, Z. W. Huangfu, S. Z. Tan, Z. L. Wang and W. J. Mai, *Nano Energy*, 2022, **104**, 107941.
143 X. Y. Lu, Y. Q. Li, D. R. Dong, Y. B. Wan, R. P. Li, L. H. Xiao, D. Wang, L. L. Liu, G. Z. Wang, J. Q. Zhang, M. Z. An and P. X. Yang, *J. Colloid Interface Sci.*, 2024, **653**, 654–663.
144 Y. Y. Jiao, X. K. Gu, P. B. Zhai, Y. Wei, W. Liu, Q. Chen, Z. L. Yang, J. H. Zuo, L. Wang, T. F. Xu and Y. J. Gong, *Nano Lett.*, 2022, **22**, 7386–7393.
145 X. Zhang, P. Yu, G. Y. Xing, Y. Xie, X. X. Zhang, G. Y. Zhang, F. F. Sun and L. Wang, *Small*, 2022, **18**, 2205228.
146 H. S. Kim, J. Lee, J. H. Jang, H. Jin, V. K. Paidi, S. H. Lee, K. S. Lee, P. Kim and S. J. Yoo, *Appl. Surf. Sci.*, 2021, **563**, 150208.
147 Q. Yang, R. M. Liu, Y. A. Pan, Z. Cao, J. B. Zuo, F. Qiu, J. Yu, H. O. Song, Z. W. Ye and S. P. Zhang, *Cryst. Growth Des.*, 2023, **23**, 5720–5731.
148 C. X. Xu, J. X. Wu, L. Chen, Y. Gong, B. Y. Mao, J. C. Zhang, J. H. Deng, M. X. Mao, Y. Shi, Z. H. Hou, M. X. Cao, H. X. Li, H. H. Zhou, Z. Y. Huang and Y. F. Kuang, *Energy Environ. Mater.*, 2024, **7**, 12569.
149 R. S. Li, C. S. Gu, P. Rao, P. L. Deng, D. X. Wu, J. M. Luo, J. Li, Z. P. Miao, C. W. Zheng, C. Shen and X. L. Tian, *Chem. Eng. J.*, 2023, **468**, 143641.
150 S. Liang, L. C. Zou, L. J. Zheng, F. Li, X. X. Wang, L. N. Song and J. J. Xu, *Adv. Energy Mater.*, 2022, **12**, 2103097.

151 J. M. Guo, W. Q. Li, Y. C. Xu, Y. Q. Mao, Z. W. Mei, H. H. Li, Y. He, X. Y. San, K. Xu and X. G. Liang, *Small Methods*, 2023, **7**, 2201371.
152 J. Rong, E. R. Gao, N. C. Liu, W. Y. Chen, X. S. Rong, Y. Z. Zhang, X. D. Zheng, H. S. Ao, S. L. Xue, B. Huang, Z. Y. Li, F. X. Qiu and Y. T. Qian, *Energy Storage Mater.*, 2023, **56**, 165–173.
153 H. W. Choi, H. Lee, J. Lu, S. Bin Kwon, D. I. Jeong, B. J. Park, J. Kim, B. K. Kang, G. Jang, D. H. Yoon and H. S. Park, *Carbon Energy*, 2024, **6**, 505.
154 J. J. Chen, S. Gu, R. Hao, Z. Y. Wang, M. Q. Li, Z. Q. Li, K. Liu, K. M. Liao, Z. Q. Wang, H. Huang, Y. Z. Li, K. L. Zhang and Z. G. Lu, *Rare Met.*, 2022, **41**, 2055–2062.
155 X. Y. Yao, Y. Q. Zhu, T. Y. Xia, Z. L. Han, C. L. Du, L. F. Yang, J. C. Tian, X. L. Ma, J. H. Hou and C. B. Cao, *Small*, 2023, **19**, 2301075.
156 L. Yan, L. Y. Xie, X. L. Wu, M. Y. Qian, J. R. Chen, Y. J. Zhong and Y. Hu, *Carbon Energy*, 2021, **3**, 856–865.
157 T. T. Cui, Y. P. Wang, T. Ye, J. Wu, Z. Q. Chen, J. Li, Y. P. Lei, D. S. Wang and Y. D. Li, *Angew. Chem., Int. Ed.*, 2022, **61**, 202115219.
158 D. C. Duan, J. L. Huo, J. X. Chen, B. Chi, Z. S. Chen, S. H. Sun, Y. Zhao, H. Zhao, Z. M. Cui and S. J. Liao, *Small*, 2024, **20**, 2310491.
159 H. Y. Zuo, Z. Y. Zhao, Y. He, S. Li, X. P. Li, Z. H. Cheng, C. Cheng, A. Thomas and Y. Z. Liao, *Carbon*, 2023, **201**, 984–990.
160 M. J. Wang, L. Wang, Q. B. Li, D. Wang, L. Yang, Y. J. Han, Y. Ren, G. Tian, X. Y. Zheng, M. W. Ji, C. Z. Zhu, L. S. Peng and G. I. N. Waterhouse, *Small*, 2023, **19**, 2300373.
161 Y. Zhang, X. Y. Gao, Z. Wen, C. C. Yang and Q. Jiang, *Chem. Eng. J.*, 2022, **446**, 137441.
162 J. J. Ban, X. H. Wen, H. J. Xu, Z. Wang, X. H. Liu, G. Q. Cao, G. S. Shao and J. H. Hu, *Adv. Funct. Mater.*, 2021, **31**, 2010472.
163 P. Li, H. L. Wang, X. H. Tan, W. Hu, M. H. Huang, J. Shi, J. W. Chen, S. Liu, Z. C. Shi and Z. Li, *Appl. Catal., B*, 2022, **316**, 121674.
164 T. Gu, D. Zhang, Y. Yang, C. Peng, D. Xue, C. Zhi, M. Zhu and J. Liu, *Adv. Funct. Mater.*, 2023, **33**, 2212299.
165 Z. H. Chen, X. W. Peng, Z. X. Chen, T. Z. Li, R. Zou, G. Shi, Y. F. Huang, P. Cui, J. Yu, Y. L. Chen, X. Chi, K. P. Loh, Z. Q. Liu, X. H. Li, L. X. Zhong and J. Lu, *Adv. Mater.*, 2023, **35**, 2209948.
166 W. X. Liu, X. X. Niu, J. X. Feng, R. L. Yin, S. L. Ma, W. B. Que, J. L. Dai, J. W. Tang, F. F. Wu, W. H. Shi, X. J. Liu and X. H. Cao, *ACS Appl. Mater. Interfaces*, 2023, **15**, 15344–15352.
167 S. Y. Lin, X. Zhang, S. Y. Sang, L. Zhang, J. J. Feng and A. J. Wang, *J. Colloid Interface Sci.*, 2022, **628**, 499–507.
168 Z. Li, M. Chen, L. Zhang, R. Xing, J. Hu, X. Huang, C. Zhou, Y. Zhou, T. Wågberg and G. Hu, *J. Mater. Chem. A*, 2023, **11**, 2155–2167.
169 H.-S. Fan, F.-X. Ma, Z.-H. Liu, W.-H. Wang, Z.-Q. Liu, X.-Y. Liang, Y. Du, Y.-Y. Li, L. Zhen and C.-Y. Xu, *Rare Met.*, 2024, **43**, 5769–5780.
170 C. Sun, Y.-J. Zhao, X.-Y. Yuan, J.-B. Li and H.-B. Jin, *Rare Met.*, 2022, **41**, 2616–2623.
171 A. S. Wang, X. L. Zhang, S. Gao, C. N. Zhao, S. Y. Kuang, S. S. Lu, J. T. Niu, G. Wang, W. F. Li, D. Chen, H. J. Zhang, X. M. Zhou, S. Zhang, B. Zhang and W. C. Wang, *Adv. Mater.*, 2022, **34**, 2204247.
172 J. J. Cai, H. J. Liu, Y. L. Luo, Y. Q. Xiong, L. Z. Zhang, S. Wang, K. Xiao and Z. Q. Liu, *J. Energy Chem.*, 2022, **74**, 420–428.
173 Z. Peng, H. T. Wang, X. C. Xia, X. X. Zhang and Z. H. Dong, *ACS Sustainable Chem. Eng.*, 2020, **8**, 9009–9016.
174 C. Zhang, X. Wang, K. Song, K. Chen, S. Dai, H. Wang and M. Huang, *Nano Res.*, 2023, **16**, 9371–9378.
175 M. J. Wu, G. X. Zhang, Y. F. Hu, J. Wang, T. X. Sun, T. Regier, J. L. Qiao and S. H. Sun, *Carbon Energy*, 2021, **3**, 176–187.
176 S. M. Chang, H. Zhang and Z. Y. Zhang, *J. Energy Chem.*, 2021, **56**, 64–71.
177 Y. L. Wu, Z. X. Xiao, Z. C. Jin, X. Y. Li and Y. L. Chen, *J. Colloid Interface Sci.*, 2021, **590**, 321–329.
178 J. Zheng, G. Hu, B. Liu, Y. Liu, H. Li, H. Zhao and M. Yang, *Energy Storage Mater.*, 2024, **65**, 103106.
179 S. J. Ha, J. Hwang, M. J. Kwak, J. C. Yoon and J. H. Jang, *Small*, 2023, **19**, 2300551.
180 S. Liu, Z. Sun, Y. Guo, F. Zheng, B. Nan, W. Kang, K. Qu, L. Wang, R. Li, Z. Li, S. Xiong and H. Li, *Inorg. Chem. Front.*, 2023, **10**, 6245–6252.
181 M. Q. Pan, Y. W. Yu, Z. Zhang, Z. Q. An and X. L. Hu, *Appl. Surf. Sci.*, 2023, **638**, 158070.
182 F. F. Chang, H. N. Du, P. P. Su, Y. H. Sun, R. P. Ye, Q. Tian, G. X. Zhang, H. T. Li and J. Liu, *Small Struct.*, 2024, **5**, 2300111.
183 X. Y. Dong, Z. H. Yao, Y. T. Li, J. Wang and Q. Zhong, *ChemistrySelect*, 2023, **8**, e202203929.
184 X. T. Han, N. N. Li, J. S. Baik, P. X. Xiong, Y. B. Kang, Q. Y. Dou, Q. Liu, J. Y. Lee, C. S. Kim and H. S. Park, *Adv. Funct. Mater.*, 2023, **33**, 2212233.
185 W. Guo, F. Gu, Q. Chen, K. Fu, Y. Zhong, J. J. Lv, S. Pan and Y. Chen, *Carbon Energy*, 2024, **567**, e567.
186 L. Ye, W. Chen, Z. J. Jiang and Z. Jiang, *Carbon Energy*, 2024, **6**, e457.
187 X.-L. Hu, J.-C. Fan, X. Li, Z.-K. Wu, Y.-Y. Li and C.-H. Xu, *Rare Met.*, 2024, **43**, 4961–4972.
188 X. Xu, Y. Pan, Y. Zhong, C. Shi, D. Guan, L. Ge, Z. Hu, Y. Y. Chin, H. J. Lin, C. T. Chen, H. Wang, S. P. Jiang and Z. Shao, *Adv. Sci.*, 2022, **9**, e2200530.
189 T. Y. Zhang, Z. N. Wang, A. P. Zhu and F. Ran, *Electrochim. Acta*, 2020, **348**, 136312.
190 Z. P. Wu, Y. L. Wang, X. B. Liu, C. Lv, Y. S. Li, D. Wei and Z. F. Liu, *Adv. Mater.*, 2019, **31**, 1800716.
191 C. Cheng, C. Zhi, Z.-T. Sun, Y.-Q. Ming, T.-T. Xiang, Q.-C. Zhu, Z.-R. Wu, B. Li, Y. Li, C. Jin, Y. Cao and J. Yang, *Rare Met.*, 2024, **43**, 1524–1536.
192 Q. C. Liu, Z. W. Chang, Z. J. Li and X. B. Zhang, *Small Methods*, 2018, **2**, 1700231.

193 S.-Q. Li, K. Sun, Y.-Y. Liu, S.-L. Liu, J.-J. Zhou, W.-B. Zhang, Y.-H. Lu, X.-M. Chen, X.-P. Wang, B.-J. Li and J.-C. Jiang, *Rare Met.*, 2024, **43**, 4982–4991.
194 T. V. Tam, S. G. Kang, M. H. Kim, S. G. Lee, S. H. Hur, J. S. Chung and W. M. Choi, *Adv. Energy Mater.*, 2019, **9**, 1900945.
195 H. J. Qiu, P. Du, K. L. Hu, J. J. Gao, H. L. Li, P. Liu, T. Ina, K. Ohara, Y. Ito and M. W. Chen, *Adv. Mater.*, 2019, **31**, 1900843.
196 D. X. Ji, L. Fan, L. L. Li, S. J. Peng, D. S. Yu, J. N. Song, S. Ramakrishna and S. J. Guo, *Adv. Mater.*, 2019, **31**, 1808267.
197 Z. H. Pan, J. Yang, W. J. Zang, Z. K. Kou, C. Wang, X. Y. Ding, C. Guan, T. Xiong, H. Chen, Q. C. Zhang, Y. T. Zhong, M. N. Liu, L. D. Xing, Y. C. Qiu, W. S. Li, C. L. Yan, Y. G. Zhang and J. Wang, *Energy Storage Mater.*, 2019, **23**, 375–382.
198 M. Yu, F. Guo, L. Xu, Y. Zhang, W. Ni, J. Wang, Y. Wei, X. Chen, J. Yang, H. Li, J. Wang and J. Wang, *Adv. Funct. Mater.*, 2024, 2411935, DOI: **10.1002/adfm.202411935**.
199 Y. Shen, H. Mao, C. Li, K. Li, Y. Liu, J. Liao, S. Zhang, Y. Fang and X. Cai, *Adv. Fiber Mater.*, 2024, **6**, 1470–1482.
200 S. Qu, J. Liu, X. Han, Y. Deng, C. Zhong and W. Hu, *Carbon Energy*, 2022, **4**, 867–877.
201 X. Tang, Y. Wang, Z. Zhang, M. Xu, Z. Tao, S. Li, J. Liu, Z. Peng, C. Guo, L. He, R. Wang, M. Du, Z. Zhang and S. H. Kim, *Nano Energy*, 2024, **127**, 109713.
202 X. Liu, Z. Wang, J. Wang, T. Tang, C. Li, J. Yu, S. Zhang and C. Deng, *Energy Storage Mater.*, 2024, **65**, 103184.
203 A. Li, Y. Wang and C. Cheng, *Mater. Today Nano*, 2023, **22**, 100339.
204 Y. Zhang, X. Zhang, Y. Li, J. Wang, S. Kawi and Q. Zhong, *Nano Res.*, 2023, **16**, 6870–6880.
205 Y. Ye, L. Zhang, Q. Zhu, Z. Du, T. Wagberg and G. Hu, *J. Colloid Interface Sci.*, 2023, **650**, 1350–1360.
206 N. Shang, K. L. Wang, M. H. Wei, Y. Y. Zuo, P. F. Zhang, H. W. Wang, Z. Chen, D. Y. Zhong and P. C. Pei, *Adv. Funct. Mater.*, 2023, **33**, 2303719.
207 S. Gao, K. Lian, X. Wang, X. Liu, A. Abdukayum, Q. Kong and G. Hu, *Small*, 2024, 2406776, DOI: **10.1002/smll.202406776**.
208 D. Qin, J. Ding, C. Liang, Q. Liu, L. Feng, Y. Luo, G. Hu, J. Luo and X. Liu, *Acta Phys.-Chim. Sin.*, 2024, **40**, 2310034.
209 M. Jiao, L. Dai, H. R. Ren, M. Zhang, X. Xiao, B. Wang, J. Yang, B. Liu, G. Zhou and H. M. Cheng, *Angew. Chem., Int. Ed.*, 2023, **62**, 202301114.
210 M. Chen, J. Ma, C. Chen, J. Ding, Y. Liu, H. He, Q. Liu, G. Hu, Y. Wu and X. Liu, *Chem. Eng. J.*, 2024, **498**, 155302.